# A New Multiresolution CYGNSS Data Product for Fully and Partially Coherent Scattering

Hugo Carreno-Luengo, *Senior Member, IEEE*, Christopher S. Ruf, *Life Fellow, IEEE*, Scott Gleason, *Senior Member, IEEE*, and Anthony Russel

***Abstract*— A new Cyclone Global Navigation Satellite System (CYGNSS) data product is described, which is generated from the raw intermediate frequency (IF) data. The product includes several established signal coherence detectors, including the power ratio $P_{\text{ratio}}$, complex zero-Doppler delay waveform, full entropy $E_{\text{full}}$, and a novel fast entropy detector $E_{\text{fast}}$. Both entropy detectors are provided with two temporal resolutions: 2 and 50 ms. Coherence performance is characterized using the phase derivative of the reflected signal at the peak of the delay waveform $\varphi_{\text{peak}}$. Threshold values of the full entropy detector are determined, which classify scattering into three regimes: incoherent, partially coherent, and coherent. Several scattered signal strength products are included: signal-to-noise ratio (SNR), reflected power $P_g$, reflectivity $\Gamma$, and normalized bistatic radar cross section (NBRCS). Each of these products is derived using a coherent integration time of $T_c = 1$ ms and incoherent integration times of $N_{\text{inc}} = 1000$, 500, 250, 100, 50, and 2 ms. Signal strength time series at the shorter (2 and 50 ms) times provides excellent detection of land–water transitions in heterogeneous scenes. Delay Doppler maps (DDMs) are also generated with high delay ($\Delta\tau = 1/16$ chip) and Doppler ($\Delta f = 50$ Hz) resolution. The behavior of each signal strength product as a coherence detector is examined using the full entropy method as a reference. Performance is characterized using receiver operating characteristic (ROC) curves. The fast entropy method, which has a much lower computational cost, is similarly characterized. This suite of coherence detection methods can be used to detect the presence of small inland water bodies.**

***Index Terms*— Coherent and incoherent scattering, Cyclone Global Navigation Satellite System (CYGNSS), Global Navigation Satellite System Reflectometry (GNSS-R), inland water detection, raw intermediate frequency (IF).**

## I. Introduction

THE Cyclone Global Navigation Satellite System (CYGNSS) mission [1], [2] is the first microsatellite constellation by the National Aeronautics and Space Administration (NASA). CYGNSS provides high spatiotemporal sampling capabilities for Earth's science studies using Earth's surface reflected global positioning system (GPS) L-band signals at left-hand circular polarization (LHCP). The mission was originally proposed to further advance extreme weather predictions with a focus on tropical cyclone (TC) inner core process studies. More recently, the mission scientific goals were extended for land surface studies, including soil moisture content (SMC) determination, e.g., [3] and [4], surface water monitoring, e.g., [5], [6], and [7], and freeze/thaw detection, e.g., [8]. The CYGNSS Global Navigation Satellite System Reflectometry (GNSS-R) mission team, e.g., [9], [10], [11], [12], [13], [14], [15], and [16], has developed several L1, L2, and L3 nominal products, which are publicly available through the NASA's Physical Oceanography Distributed Active Archive Center (PODAAC).

In addition, CYGNSS captures raw intermediate frequency (IF) signal tracks, e.g., [17], [18], and [19], over specific Earth's surface areas (see Fig. 1). The main foundation of this CYGNSS raw IF calibrated product is on the generation of improved quality high-resolution delay Doppler maps (DDMs) with shorter integration times, using all the available raw IF tracks collected over land surfaces. This multiresolution product is currently available for the CYGNSS inundation working group. It offers a unique opportunity for studies dedicated to, e.g., river width [20], river slope [21], wetlands [22], floods [23], single pass SMC retrievals [24], and development and validation of new GNSS-R scattering models, e.g., [25] and [26]. This scenario also offers the possibility to test and develop new GNSS-R opportunities in preparation for the future European Space Agency (ESA) HydroGNSS

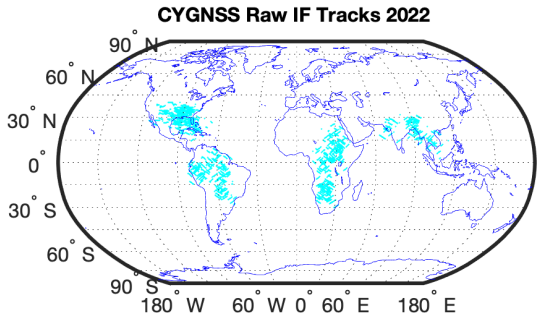



Fig. 1. Geodistribution of the 2022 CYGNSS Earth's land surface raw IF tracks. Target areas cover mainly tropical rainforest regions, as well as Southern USA, Sudan, India, and Vietnam. Specific sites were selected by the CYGNSS Science Team based on scientific requirements for ongoing and future investigations.

Manuscript received 5 June 2023; revised 21 August 2023; accepted 17 September 2023. Date of publication 25 September 2023; date of current version 6 October 2023. This work was supported by the NASA Science Mission Directorate under Grant 80LARC21DA003 with the University of Michigan (UMich). *(Corresponding author: Hugo Carreno-Luengo.)*

Hugo Carreno-Luengo, Christopher S. Ruf, and Anthony Russel are with the Department of Climate and Space Sciences and Engineering, University of Michigan, Ann Arbor, MI 48109 USA (e-mail: carreno@umich.edu; cruf@umich.edu; russelan@umich.edu).

Scott Gleason is with Daaxa LLC, Boulder, CO 80307 USA (e-mail: sgleason@protonmail.com).

Digital Object Identifier 10.1109/TGRS.2023.3318639

© 2023 The Authors. This work is licensed under a Creative Commons Attribution 4.0 License.
For more information, see https://creativecommons.org/licenses/by/4.0/

microsatellite constellation mission [27], which is focused on land surface studies and plans to include an onboard coherent channel to continuously collect peak-DDM complex data and raw IF tracks over areas of interest.

Earth's surface water monitoring is probably one of the most promising applications of GNSS-R missions because of their high spatiotemporal sampling capabilities and the high spatial resolution under the coherent scattering regime. This is an important research question, and it deserves further investigation. Theoretically, the resolution is limited by the size of the first Fresnel zone, with a nonnegligible influence of higher order zones, e.g., [28], [29], [30], [31], and [32]. It was found that short $N_{\text{inc}}$ provides a reasonable tradeoff between an acceptable along-track spatial resolution and a reduced signal noise level, which enables to detect land–water transitions accurately [33]. We encourage the users to investigate this, and additional research questions, to further advance our understanding of the ultimate capabilities of GNSS-R. To do so, the product is delivered with a wide variety of observables [34], such as power DDMs ($P_g$, $\Gamma$, and BRCS), including the corresponding information at the peak $p$, as well as the normalized bistatic radar cross section (NBRCS), and a wide variety of coherence detectors, i.e., complex delay waveforms, $\varphi_{\text{peak}}$, $P_{\text{ratio}}$, $E_{\text{full}}$,and $E_{\text{fast}}$. In addition, quality flags (see the Appendix) and a comprehensive set of metadata, e.g., Moderate Resolution Imaging Spectroradiometer (MODIS) land cover type, multiresolution Pekel water masks, and topographic roughness, are included.

This article is organized as follows. First, we introduce the CYGNSS raw IF data in Section II. Then, the raw IF signal processing is presented in Section III, describing the details of the enhanced DDMs, the signal calibration approach, and the derived land surface observables. Then, the coherence detectors are presented and described in Section IV. Finally, Section V concludes this article.

## II. CYGNSS Raw IF Data

### A. Introduction

The raw IF samples collected by the delay Doppler mapping instrument (DDMI) onboard CYGNSS contain the highest possible resolution over delay and Doppler space. The access to this raw IF data enables high-resolution processing on-ground, in many ways not possible in real time by the instrument. For example, the raw IF samples can be processed to extract in-phase $I$ and quadrature $Q$ information of the complex DDMs for high-quality evaluation of coherent Earth's surface scattering. In addition, comprehensive studies of the received reflected signal power can be performed using variable delay and Doppler spacing and integration times, thus permitting the generation of extremely high-resolution DDMs for advanced science applications, including ocean and land.

### B. Baseline L1 Mission Product

After the antenna and the low-noise amplifier (LNA), the GPS signal enters the onboard receiver, where it is downconverted and digitized. These raw IF samples are then processed using a fast Fourier transform (FFT) technique, implemented in the receiver. The real-time output is a DDM with 128 delay bins at 1/4 chip delay steps and 20 Doppler bins at 500-Hz steps. The scattered signal power is processed using a coherent integration time $T_c = 1$ ms and an incoherent averaging time $N_{\text{inc}} = 1000$ ms (December 2016–August 2019) or 500 ms (August 2019–present). This onboard full DDM is compressed to meet the satellite downlink requirements. The compressed DDM includes 17 delay bins and 11 Doppler bins, which are centered at the onboard estimated nominal specular point, and the bit depth of each bin is truncated from 32 to 8 bits. A more precise geolocation of the nominal specular point is performed on-ground. These DDMs are generated in raw uncalibrated units, and calibration is performed at the University of Michigan (UMich) [35].

### C. Raw IF Data Collection

Starting from 2017, some few raw IF datasets are being collected by the DDMI and downloaded to ground for improved studies over specific target areas, with specific interest for the CYGNSS science team. More recently, a new raw IF data collection strategy was approved in winter 2022 so that ~20 raw IF tracks are downloaded continuously every week. Two files for each raw IF data collection are generated: one raw IF metadata file and one raw IF data file. The raw IF metadata file contains the ID of the spacecraft, a single Data Recorder Track 0 (DRT0) packet, and one or more pulse per second (PPS) packets. The raw IF data file includes three sets of raw signal sample streams (~60 s) received by the zenith antenna and the nadir antennas at port and starboard. All raw IF tracks collected by the CYGNSS mission to date include byte interleaved data from all three antenna channels of the DDMI, numbered as follows: zenith navigation antenna, nadir starboard side science antenna, and nadir port side science antenna.

All samples for all channels are saved as 2-bit values and are interleaved. The source of the binary raw IF data is byte 9–byte $N$ of the File Transfer Packet Data (FD00) packets emitted by the DDMI. The raw IF file contains bytes 9–$N$ of multiple contiguous FD00 packets. The FD00 packets are expected to contain consecutive sequence byte numbers. If a missing FD00 packet is detected, 2048 zero bytes are inserted in the raw IF file in place of the missing data. The first FD00 packet in the stream carries a DRT0 header block at the beginning of the data bytes. The rest of this first packet and all subsequent packets contain the binary raw IF sample data.

## III. Raw IF Signal Processing

### A. Introduction

The bandwidth of the raw signal is ~2.5 MHz, centered at the IF of ~3.8 MHz. In the nominal mode, the IF signals are sampled with a sampling rate of ~16.0 MHz and a resolution of 2 bits per sample for both direct and reflected channels. The ground-based raw IF processing uses a delay-domain FFT technique to perform the correlations at all the delay samples using a frequency-domain multiplication. The delay sampling is configured based on the decimation of the sampling rate and

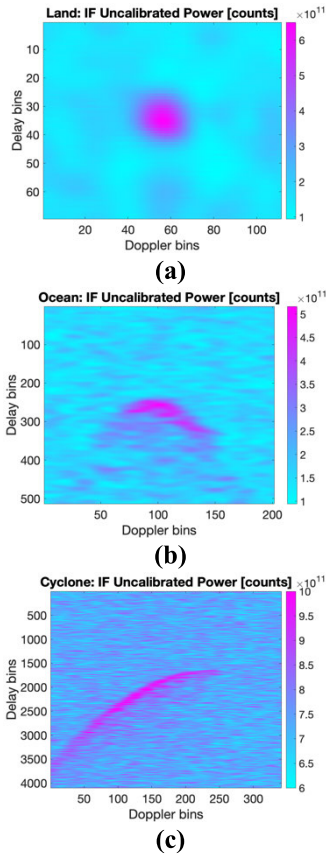



Fig. 2. Enhanced uncalibrated DDMs [$\Delta f = 50$ Hz Doppler bin resolution and $\Delta\tau = 1/16$ chip delay bin resolution] derived from the raw IF processing in counts: (a) standard DDM—land ($N_{\text{inc}} = 50$ ms), (b) full DDMs—ocean ($N_{\text{inc}} = 50$ ms), and (c) super DDMs—cyclone ($N_{\text{inc}} = 250$ ms). The antenna footprint on the surface often truncates one side of the signal [see Fig. 2(c)].

the Doppler processing range. $N_{\text{inc}}$ and the delay Doppler sampling properties are also configured depending on the Earth's surface type, i.e., ocean versus land. The raw IF processing is designed and built on a Linux Ubuntu laptop using the GNU Compiler Collection (GCC) compiler and the FFTW library. The code is written in C with the FFT processing based on the open source "fastgps" signal acquisition processor [36], upgraded to accept the CYGNSS raw IF data format and perform GNSS-R specific processing tasks, including variable noncoherent integration.

### B. Multiresolution Enhanced DDMs

Different types of enhanced DDMs can be generated to improve and enable new scientific applications over land and ocean by CYGNSS (see Table I). The main three DDM types are illustrated in Fig. 2. In so doing, the key parameters are the following: coherent integration time $T_c$, incoherent integration time $N_{\text{inc}}$, delay bin resolution $\Delta\tau$, Doppler bin resolution $\Delta f$, delay window $d_w$, and Doppler window $D_w$. This article is focused on Earth's land surfaces [see Fig. 2(a)].

All enhanced DDMs are generated with $\Delta f = 50$-Hz Doppler bin resolution and $\Delta\tau = 1/16$ chip delay bin resolution. The DDMI estimation of the Doppler at the nominal specular point is introduced in the raw IF processing to reproduce as much as possible the onboard scenario for calibration

TABLE I

SUMMARY OF THE PROPERTIES OF EACH RAW IF DATA PRODUCT TYPE. THIS ARTICLE IS FOCUSED ON LAND. COHERENT INTEGRATION TIME $T_c$, INCOHERENT INTEGRATION TIME $N_{\text{inc}}$, DELAY BIN RESOLUTION $\Delta\tau$, DOPPLER BIN RESOLUTION $\Delta f$, DELAY WINDOW $d_w$, AND DOPPLER WINDOW $D_w$

| | $T_c$ [ms] | $N_{inc}$ [ms] | $\Delta\tau$ [chips] | $\Delta f$ [Hz] | $d_w$ [bins] | $D_w$ [bins] |
|---|---|---|---|---|---|---|
| **Land** | 1 | 1000, 500,250, 100, 50,2 | 1/16 | 50 | 69 | 111 |
| **Ocean** | 1 | 1000, 500,250, 100,50 | 1/16 | 50 | 513 | 201 |
| **Cyclone** | 1 | 1000, 500, 250 | 1/16 | 50 | 4097 | 401 |

purposes. The DDMI Doppler information is provided every $N_{\text{inc}} = 1000$ ms (December 2016–August 2019) or every $N_{\text{inc}} = 500$ ms (August 2019–present). A spline method is applied to the DDMI-based Doppler vector to generate more precise Doppler inputs for lower integration times $N_{\text{inc}} = 250$ ms, $N_{\text{inc}} = 100$ ms, $N_{\text{inc}} = 50$ ms, and $N_{\text{inc}} = 2$ ms.

The delay bin resolution is determined by the effective sampling rate. In the nominal mode, raw IF data are sampled at a rate of ~16 MHz, which is approximately 16 000 samples per 1 ms. Approximately, 16 samples per GPS coarse/acquisition (C/A) code chip is a delay chip resolution of 1/16 chip in the DDMs. The raw IF processing allows the selection of different delay bin resolutions so that the ~16-MHz samples are downsampled.

1) *1/8 Chip Delay Bin Resolution:* Downsampling by a factor of 2 to a ~8-MHz sampling rate or eight samples per chip.
2) *1/4 Chip Delay Bin Resolution:* Downsampling by a factor of 4 to a ~4-MHz sampling rate or four samples per chip.
3) *1/2 Chip Delay Bin Resolution:* Downsampling by a factor of 8 to a ~2-MHz sampling rate or two samples per chip, which is the Nyquist limit for the GPS C/A code.

The output power after raw IF processing is not exactly the same at different delay sampling rates because the processing uses 1-ms FFTs in each case on different length vectors to perform the correlations. The shorter the vector, the faster the FFT, but delay samples are thrown out. The highest achievable resolution, which has the slowest FFTs, is at the full sampling rate or 16 samples per chip (i.e., 1/16 chip delay bin resolution). As such, the use of 1/16 chip delay bin resolution without sample decimation provides the highest fidelity results. The required longer run time is not a limiting consideration because the processing is performed on-ground.

The raw IF processing output DDMs are generated in raw uncalibrated units, known as counts (see Fig. 2). There is a scale difference between these DDMs and those generated by the DDMI probably due to the onboard compression algorithm

and the fact that the DDMI uses the "Zoom" Doppler domain correlator (and possibly some internal, unknown, bit overflow shifting/scaling) [37]. This difference must be compensated. In addition, both processing chains must be referenced to the GPS absolute time. Thus, before radiometric calibration, time synchronization and scaling strategies must be defined.

### C. Time Synchronization and Geolocation

Accurate GPS timing information derived from the direct signal received by the zenith navigation antenna is used to improve the geolocation of the nominal specular point over the Earth's surface. The nominal specular point position is computed over the world geodetic system (WGS) 84 ellipsoid of reference, and then, the solution is projected over the NASA Shuttle Radar Topography Mission (SRTM) global digital elevation model. This improvement compared to the nominal mission data enables more accurate land-surface studies. The original data strategy was designed for ocean wind speed retrieval for long $N_{\text{inc}}$, and the onboard timing precision is adequate to that goal.

In addition, a lag-correlation technique is used for each pseudorandom noise (PRN) code number, to align the onboard generated time series and the raw IF-based time series, before calibration. Lag correlation is the correlation between two series where one of the series has a time lag with respect to the other. This is required to compensate for a variable temporal offset that is present between the two time series. The compensation of this offset is used to align the raw IF time series with the onboard operations in real-time processing. Time series at different $N_{\text{inc}}$ is aligned at the beginning of each sampling rate's integration period.

### D. Calibration Strategy

*1) Scaling:* Uncalibrated DDMs are measured in counts. These counts are linearly related to the total signal power generated by the raw IF processing ($C_{\text{if}}$) or the DDMI ($C_{\text{ddmi}}$).

Raw IF-based DDMs ($C_{\text{if}}$) in counts can be related to the arriving signal power as follows:

$$C_{\text{if}}(\tau, f) = G_{\text{if}}(P_a + P_r + P_g(\tau, f) + P_e) \tag{1}$$

where $\tau$ is the delay, $f$ is the Doppler, $G_{\text{if}}$ is the end-to-end gain of the raw IF processor, $P_a$ is the thermal noise power generated by the antenna (in Watts), $P_r$ is the thermal noise power generated by the instrument (in Watts), $P_g$ is the scattered GNSS power (in Watts), and $P_e$ (in Watts) represents certain parameters of the real-time signal processing performed by the DDMI on orbit, which are unknown, and so cannot be exactly duplicated by the ground processing of raw IF data.

DDMI-based DDMs ($C_{\text{ddmi}}$) in counts can be related to the arriving signal power as follows:

$$C_{\text{ddmi}}(\tau, f) = G_{\text{ddmi}}(P_a + P_r + P_g(\tau, f)) \tag{2}$$

where $G_{\text{ddmi}}$ is the end-to-end gain in real-time DDMI processing.

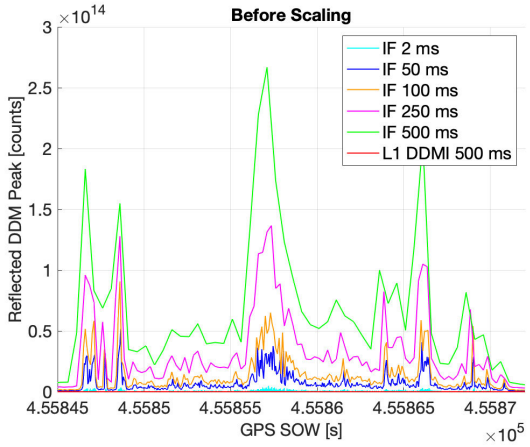



Fig. 3. Before-scaling comparison of DDMI [$\Delta f = 500$ Hz, $\Delta\tau = 1/4$ chip, and $N_{\text{inc}} = 500$ ms] and raw IF [$\Delta f = 50$ Hz and $\Delta\tau = 1/16$ chip] peak reflected-power time series [counts]. These time series correspond to a single PRN number within one raw IF file. Track acquired on April 22, 2022. The DDMI L1 (red) trace is so low that it seems to be a flat zero as its $10^5$ versus $10^{14}$ for the raw IF (see Fig. 5 for trend after scaling).

Combining (1) and (2), both types of uncalibrated DDMs can be linearly related as follows:

$$C_{\text{ddmi}}(\tau, f) = \left(\frac{G_{\text{ddmi}}}{G_{\text{if}}}\right) C_{\text{if}}(\tau, f) - G_{\text{ddmi}} P_e \tag{3}$$

The first step in the calibration is to estimate the coefficients to transform $C_{\text{if}}(\tau, f)$ in $C_{\text{ddmi}}(\tau, f)$

$$p_1 = \frac{G_{\text{ddmi}}}{G_{\text{if}}} \tag{4}$$

and

$$p_2 = -G_{\text{ddmi}} P_e \tag{5}$$

After lag correlation, a linear regression between the times series (see Fig. 3) at the maximum peak (subscript $p$) of the raw IF-based ($C_{\text{if},p}$) and the DDMI-based DDMs ($C_{\text{ddmi},p}$) at $N_{\text{inc}} = 500$ ms is used (see Fig. 4) to empirically determine the coefficients for each PRN code number per channel. This is necessary because certain parameters of the real-time signal processing performed by the DDMI on orbit are unknown and so cannot be exactly duplicated by the ground processing of raw IF data. These parameters include the start and stop times of the coherent correlation relative to the time-varying phase of the GPS L1 carrier signal and the phase tracking algorithm used to synchronize the timing of the correlator. Both parameters can affect the scaling of the DDM data products.

The scale factor is derived with the corresponding high delay and Doppler bin resolution raw IF time series [$\Delta f = 50$ Hz and $\Delta\tau = 1/16$ chip] because the output power of the raw IF processor is different at different delay sampling rates. In addition, the impact of different $N_{\text{inc}}$'s is considered. The output reflected power changes with different $N_{\text{inc}}$'s since the software processing computes an accumulation over the incoherent integration time. It does not compute an average over the incoherent integration time. Thus, there is a need to scale linearly with the length of the integration interval as

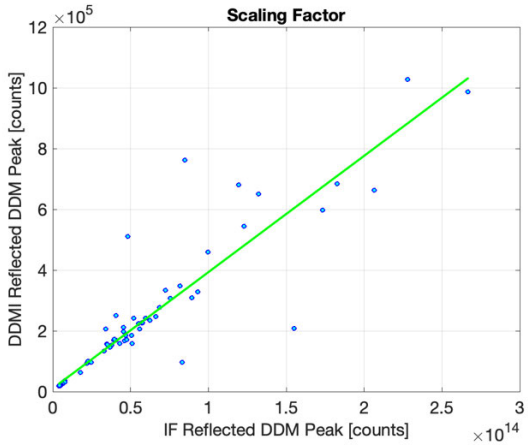



Fig. 4. Sample scale factor between DDMI [$\Delta f = 500$ Hz, $\Delta\tau = 1/4$ chip, and $N_{\text{inc}} = 500$ ms] and the $N_{\text{inc}} = 500$-ms raw IF [$\Delta f = 50$ Hz and $\Delta\tau = 1/16$ chip] time series of reflected peak power in raw uncalibrated units [counts] after lag correlation. This sample scale factor corresponds to a single PRN number within one raw IF file. Track acquired on April 22, 2022.

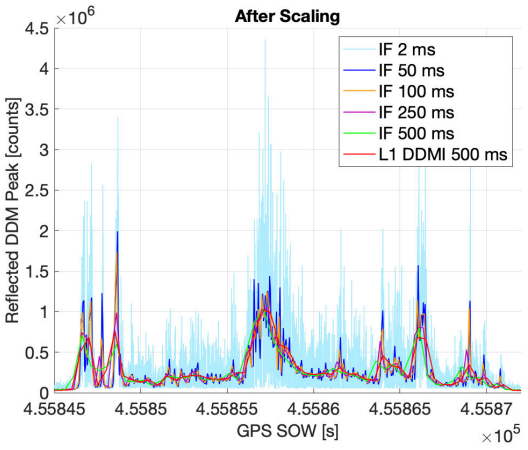



Fig. 5. After-scaling comparison of DDMI [$\Delta f = 500$ Hz, $\Delta\tau = 1/4$ chip, and $N_{\text{inc}} = 500$ ms] and raw IF [$\Delta f = 50$ Hz and $\Delta\tau = 1/16$ chip] peak reflected-power time series [counts]. These time series correspond to a single PRN number within one raw IF file. Track acquired on April 22, 2022.

follows (see Fig. 5):

$$C_{\text{if,scaled},N_{\text{inc}}}(\tau, f) = p_1 C_{\text{if},N_{\text{inc}}}(\tau, f)\frac{N_{\text{inc},0}}{N_{\text{inc}}} + p_2 \tag{6}$$

where $N_{\text{inc}}$ is any incoherent averaging and $N_{\text{inc},0}$ is the incoherent averaging time used to derive the scale factor ($p1$, $p2$), i.e., 500 ms after August 2019. It is worth highlighting that the scale factor ($p1$, $p2$) is derived for each raw IF track.

Fig. 5 shows the after-scaling time series. The output reflected power of the different time series is unbiased. In addition, the raw IF time series shows a higher dynamic range and an improved resolution compared to the DDMI because of the shorter integration times down to $N_{\text{inc}} = 2$ ms, and the higher delay and Doppler bin resolution [$\Delta f = 50$ Hz and $\Delta\tau = 1/16$ chip].

After scaling, the signal-to-noise ratio (SNR) is computed as follows:

$$\text{SNR} = 10\log 10\left(\frac{C_{\text{if},p,\text{scaled},N_{\text{inc}}}}{C_{N,\text{if,scaled},N_{\text{inc}}}}\right) \tag{7}$$

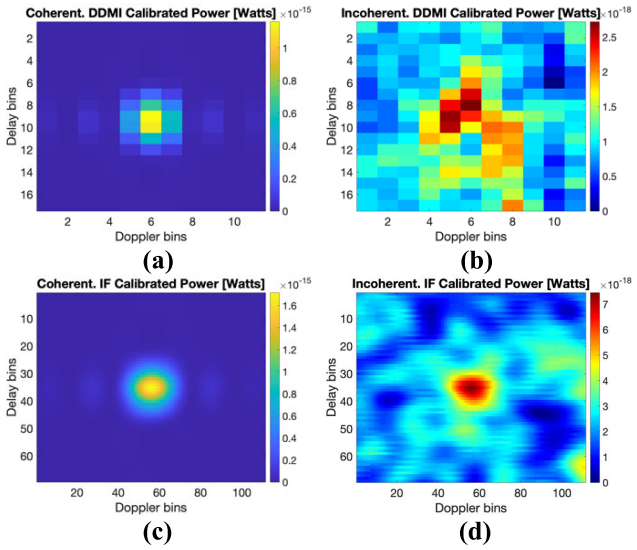



Fig. 6. Sample DDMs: (a) and (b) standard L1 DDMI data [$\Delta f = 500$ Hz, $\Delta\tau = 1/4$ chip, and $N_{\text{inc}} = 500$ ms] and (c) and (d) raw IF calibrated product [$\Delta f = 50$ Hz, $\Delta\tau = 1/16$ chip, and $N_{\text{inc}} = 50$ ms] for (a) and (c) coherent scattering regime and (b) and (d) incoherent scattering regime.

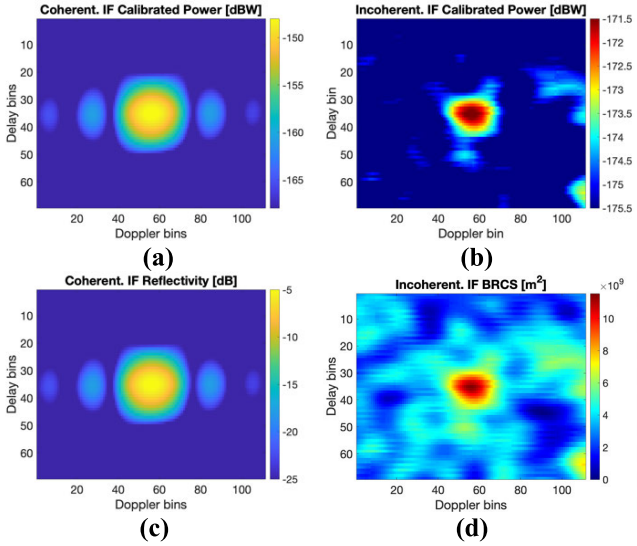



Fig. 7. Raw IF sample DDMs [$\Delta f = 50$ Hz, $\Delta\tau = 1/16$ chip, and $N_{\text{inc}} = 50$ ms] under (a) and (c) coherent scattering regime and (b) and (d) incoherent scattering regime: (a) $P_g(\tau, f)$, (b) $P_g(\tau, f)$, (c) $\Gamma(\tau, f)$, and (d) $\text{BRCS}(\tau, f)$.

where $C_{N,\text{if,scaled},N_{\text{inc}}}$ is the noise power. Noise information is calculated separately for each DDM, using pixels in which no signal power is present, i.e., the 180 top delay rows of the original uncompressed 512 × 200 DDMs [$\Delta f = 50$ Hz and $\Delta\tau = 1/16$ chip] in counts.

*2) Radiometric Calibration:* This section describes the radiometric calibration [38], [39], [40] approach used to convert each bin of the after-scaling DDMs into counts $C_{\text{if,scaled},N_{\text{inc}}}(\tau, f)$ to units of Watts $P_g(\tau, f)$. After radiometric calibration, the reflected power DDMs (in Watts) are derived as follows (see Fig. 6):

$$P_g(\tau, f) = \frac{C(P_B + P_r)}{C_B} \tag{8}$$

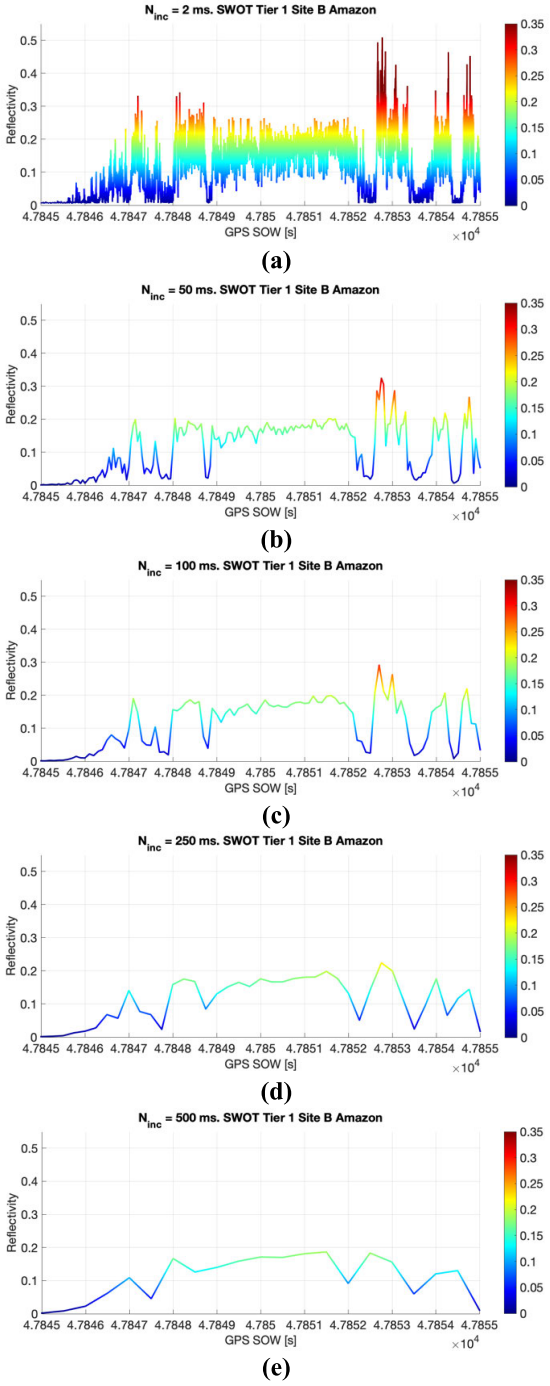



Fig. 8. GNSS-R raw IF reflectivity $\Gamma_p$ time series in the SWOT cal/val site (track acquired on March 27, 2022) for $N_{\text{inc}}$: (a) 2, (b) 50, (c) 100, (d) 250, and (e) 500 ms.

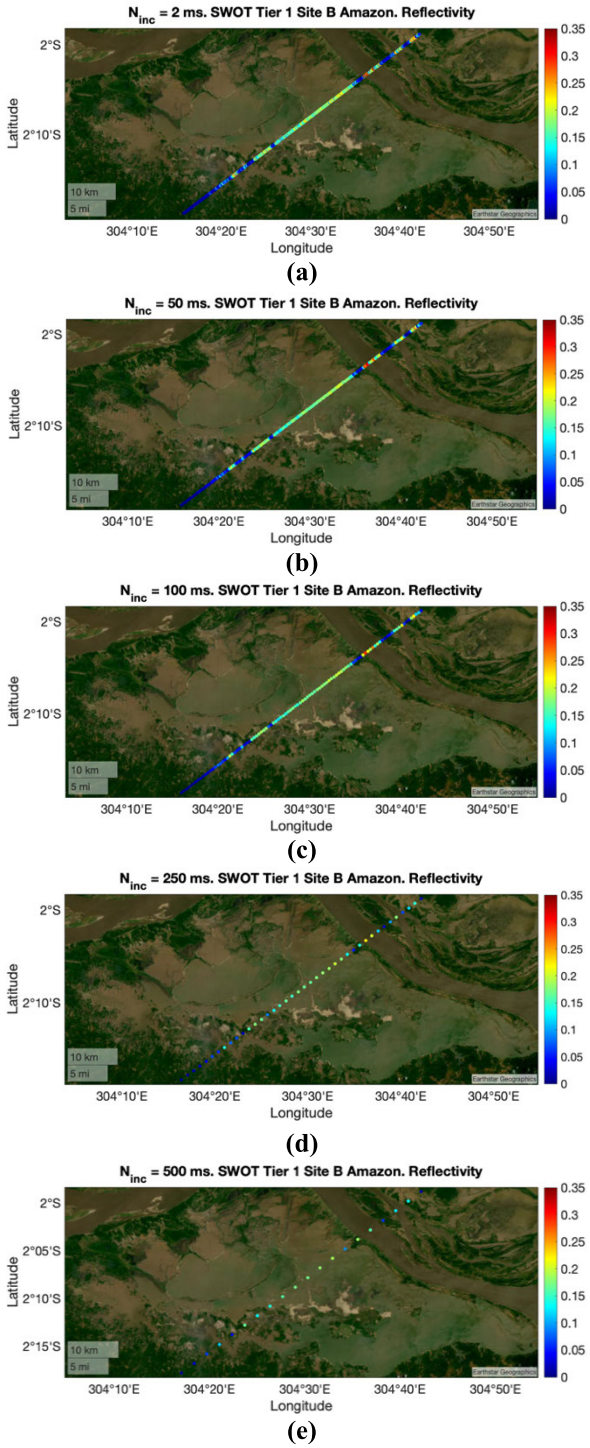



Fig. 9. GNSS-R raw IF reflectivity $\Gamma_p$ geolocated in the SWOT cal/val site (track acquired on March 27, 2022) for $N_{\text{inc}}$: (a) 2, (b) 50, (c) 100, (d) 250, and (e) 500 ms.

where $C = (C_{\text{if,scaled},N_{\text{inc}}}(\tau, f) - C_{N,\text{if,scaled},N_{\text{inc}}})$, $P_B$ is the blackbody thermal noise power, and $C_B$ is the DDM in the blackbody state.

The DDM noise power is expressed in counts as

$$C_{N,\text{if,scaled},N_{\text{inc}}} = p_1 C_{N,\text{if},N_{\text{inc}}} \frac{N_{\text{inc},0}}{N_{\text{inc}}} + p_2 \tag{9}$$

where $C_{N,\text{if},N_{\text{inc}}}$ is the noise of the before-scaling DDMs.

$P_B$ and $C_B$ are derived onboard during the blackbody calibration when a calibration switch selects between the nadir antenna and a blackbody target as the source of the input signal to the DDMI. The blackbody calibration is performed every 60 s for each nadir antenna. The DDM in the blackbody state is given as follows:

$$C_B = G(P_B + P_r) \tag{10}$$

$P_B$ can be expressed as follows:

$$P_B = kT_I B_w \tag{11}$$

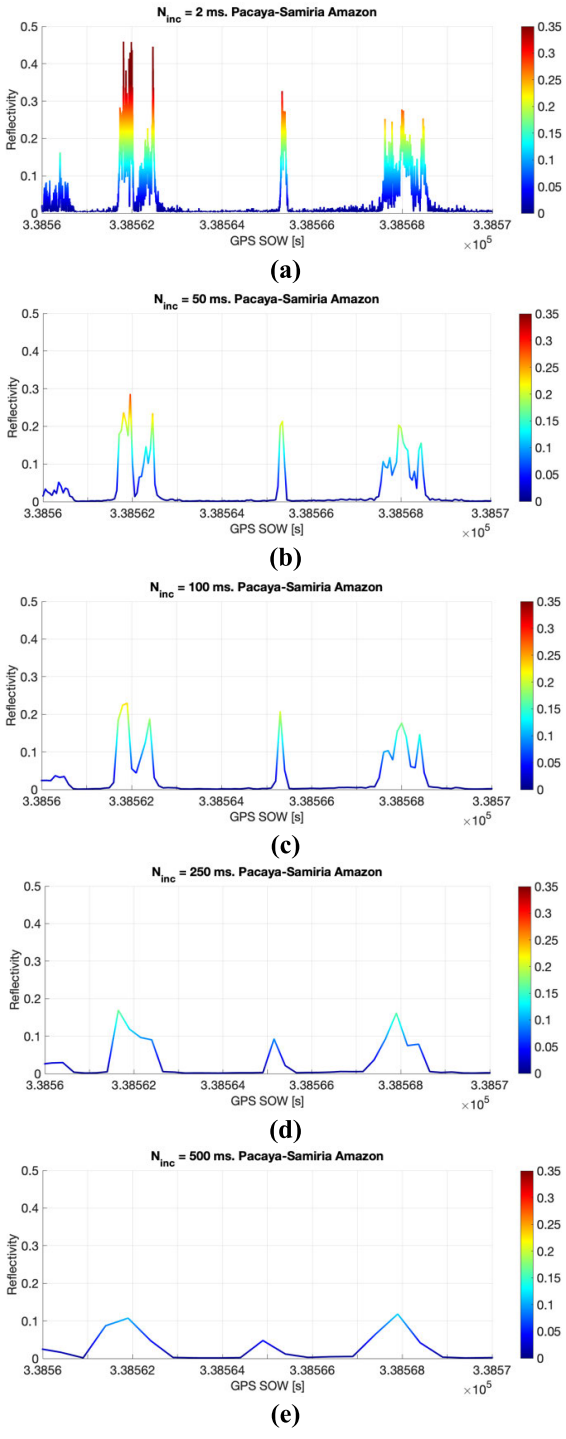



Fig. 10. GNSS-R raw IF reflectivity $\Gamma_p$ time series in Pacaya–Samiria (track acquired on February 16, 2022) for $N_{\text{inc}}$: (a) 2, (b) 50, (c) 100, (d) 250, and (e) 500 ms.

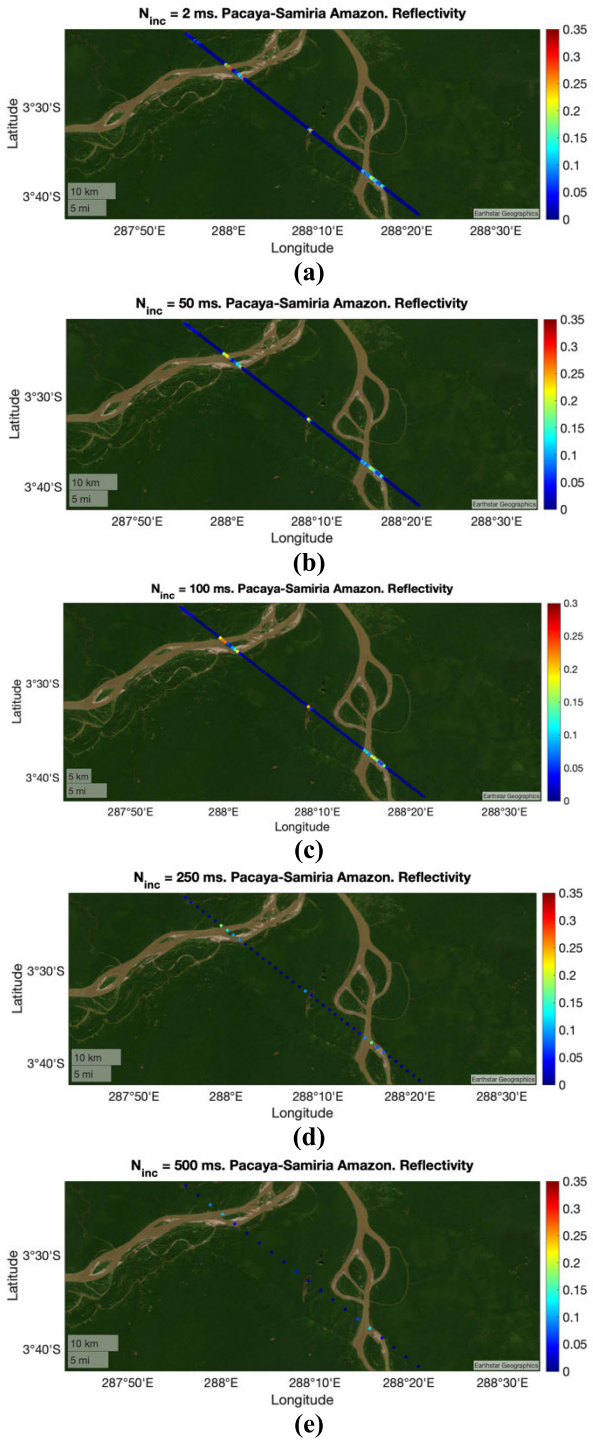



Fig. 11. GNSS-R raw IF reflectivity $\Gamma_p$ geolocated in Pacaya–Samiria (track acquired on February 16, 2022) for $N_{\text{inc}}$: (a) 2, (b) 50, (c) 100, (d) 250, and (e) 500 ms.

where $T_I$ is the effective temperature of the instrument's blackbody load source. $P_B$ is determined from a physical temperature sensor measured at 1 Hz and is near enough in time to the 1-Hz science measurement so that the physical temperature does not change significantly between the thermistor reading and the science measurement. $C_B$ is made within 10 min (starting in 2021) of science measurement and close enough in time so that the receiver gain and noise figure do not change significantly [41]. In addition, the blackbody measurements are on-ground resampled and interpolated to the measurement time.

The thermal noise power generated by the DDMI can be expressed as follows:

$$P_r = kT_r B_w = k[(\text{NF} - 1)290]B_w \tag{12}$$

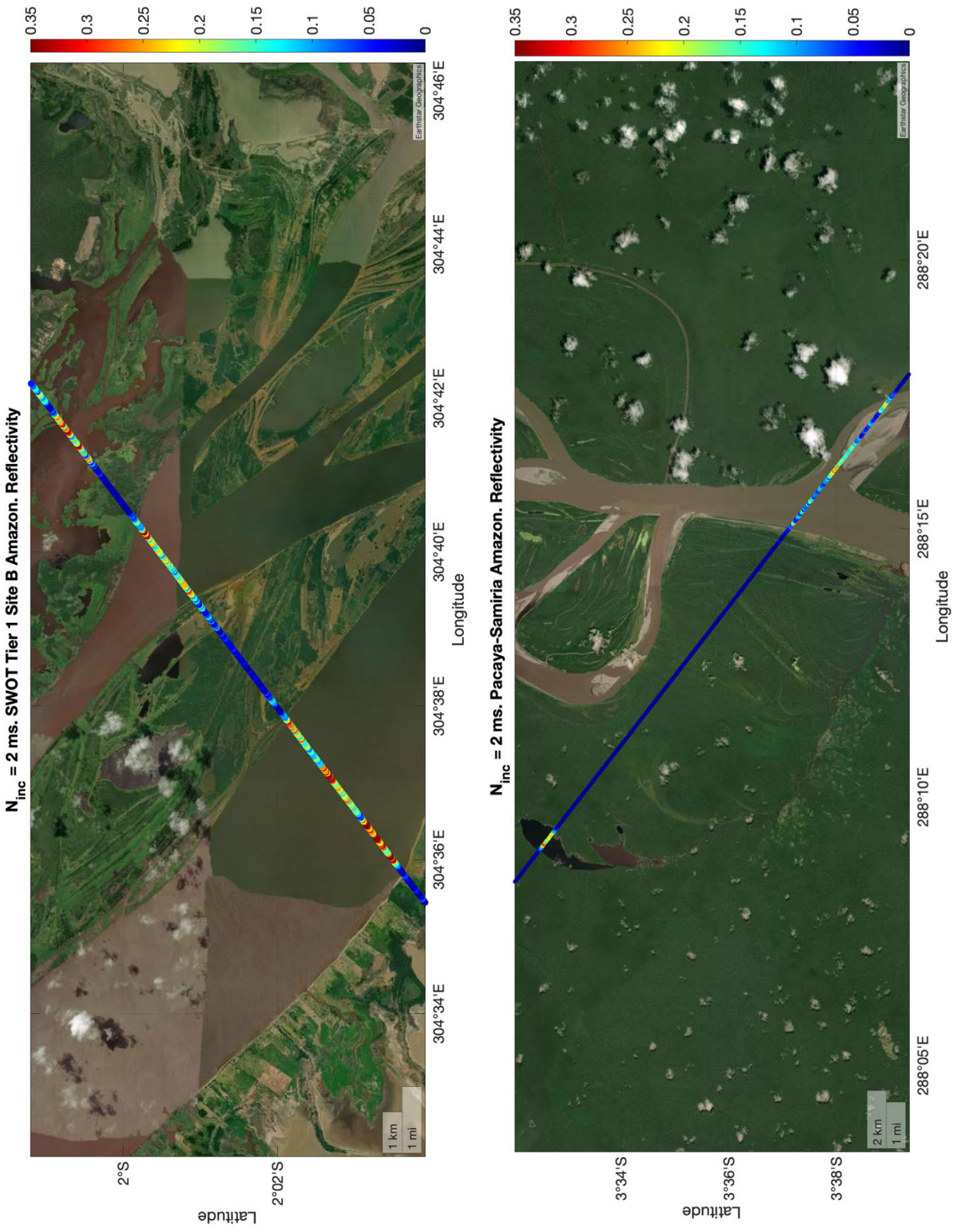



Fig. 12. Zooming GNSS-R raw IF reflectivity $\Gamma_p$ over high-interest target areas: (a) track acquired on March 27, 2022 [see Fig 9(a)] and (b) track acquired on February 16, 2022 [see Fig. 11(a)]. Land–water transitions are accurately captured by CYGNSS. Over water, the reflectivity increases because of the higher dielectric constant, smoother surface, and the absence of vegetation cover. It is also worth highlighting that the signal fluctuations over water are probably due to variable surface roughness.

where NF is the DDMI noise figure and $T_r$ is the DDMI temperature. The NF versus temperature profile was characterized prelaunch for all the instrument LNAs. NF is continuously updated in-orbit.

*3) Inverting Land Surface Parameters:* Several L1b observables are derived after radiometric calibration, including reflectivity $\Gamma(\tau, f)$, bistatic radar cross section (BRCS) $(\tau, f)$, and NBRCS$(\tau_p, f_p)$.

The reflectivity DDM is estimated as follows [see Fig. 7(c)]:

$$\Gamma(\tau, f) = \frac{(4\pi)^2 P_g(\tau, f)(R_r(\tau_p, f_p) + R_t(\tau_p, f_p))^2}{\lambda^2 G_r(\tau_p, f_p)\text{EIRP}(\tau_p, f_p)} \quad (13)$$

where $R_t$ and $R_r$ are the ranges from the transmitter and the receiver to the Earth's surface scattering area, $G_r$ is the receiver antenna gain, $\lambda$ is the signal electromagnetic wavelength, and EIRP is the transmitter equivalent isotropically radiated power of the right-hand circular polarization (RHCP) direct GPS signal.

The BRCS DDM is estimated as follows [see Fig. 7(d)]:

$$\text{BRCS}(\tau, f) = \frac{(4\pi)^3 P_g(\tau, f)(R_r(\tau_p, f_p)R_t(\tau_p, f_p))^2}{\lambda^2 G_r(\tau_p, f_p)\text{EIRP}(\tau_p, f_p)} \quad (14)$$

The surface NBRCS is estimated as follows:

$$\text{NBRCS}(\tau_p, f_p) = \frac{\text{BRCS}(\tau_p, f_p)}{A_{\text{eff}}} \quad (15)$$

where $A_{\text{eff}}$ is the effective scattering area corresponding to four delay bins × ten Doppler bins cell around the peak over land surfaces because the scattered signal is concentrated in a small area near the specular point. For the inversion of the land observables, the calibration variables are approximated with the values corresponding to the peak. This is used for the calibration of the ocean DDMs [see Fig. 2(b)] but approximating at the nominal specular point [38]. Thus, it can be applied over land surfaces because the scattering is more specular (scattered signal is concentrated in a small area near the specular point) than over the ocean. However, when the scattering is very diffuse, i.e., off-specular [see Fig. 2(c)], this approximation is no longer valid, and per-bin calibration variables must be used along the complete $d_w$ and $D_w$ windows (see Table I). In addition, the delay Doppler ambiguity introduced by the Woodward ambiguity function (WAF) must be considered.

### *E. Time Series Analysis: Reflectivity Case Study*

The time series of peak reflectivity $\Gamma_p = \Gamma(\tau_p, f_p)$ is selected to highlight some product capabilities, but more observables are available for the final users. Two IF tracks are considered over a Surface Water and Ocean Topography (SWOT) mission cal/val site (see Figs. 8 and 9) and the Pacaya–Samiria region in the Amazon basin (see Figs. 10 and 11). The corresponding geolocation of $\Gamma_p$ using Landsat imagery is depicted in Figs. 9 and 11. $N_{\text{inc}} = 2$- and 50-ms $\Gamma_p$ time series shows a higher signal dynamic range and a higher spatial resolution than those corresponding to $N_{\text{inc}} = 500$ ms. There is clear evidence of the sensitivity of $\Gamma_p$ to the presence of surface water, showing the capability to detect small inland water bodies (see Fig. 12) and land–water transitions over complex heterogeneous scenes.

In the SWOT site, low $\Gamma_p \sim$ <0.1 levels [see Fig. 8(a)] appear over vegetated areas because of the larger attenuation of the reflected signal by the vegetation cover [42], [43], [44] [see Fig. 9(a)]. On the other hand, in the inundated terrain located in one lateral of the Amazon River, $\Gamma_p$ increases up to ∼0.2. The Amazon River is then divided into several arms, surrounded by vegetation. $\Gamma_p$ can capture sharp transitions land–water–land. Within the river, there is a combination of sharp peaks $\Gamma_p \sim 0.5$ with lower values ∼0.2 probably because of the different surface roughness conditions across the wide Amazon River. It is worth pointing out that the spatial resolution gradually decreases with increasing $N_{\text{inc}}$. The 500-ms $\Gamma_p$ time series is not able to resolve this complex scene [see Fig. 9(d)]. On the other hand, increasing $N_{\text{inc}}$ helps to reduce signal noise, e.g., $N_{\text{inc}} = 2$ ms versus $N_{\text{inc}} = 50$ ms.

The Pacaya–Samiria scene (see Fig. 11) is characterized by a complex-form river within the Amazon basin, surrounded by dense vegetation and several other small-size water bodies (see Fig. 12). The orientation of the selected raw IF track is interesting because the nominal specular point crosses some of these water bodies and, in addition, is laterally surrounded by a few of them. The $N_{\text{inc}} = 2$-ms $\Gamma_p$ time series [see Fig. 11(a)] resolves this complex scene better than longer times, showing that the spatial resolution under the coherent scattering regime is fine enough to detect small inland water bodies, while the impact of higher order Fresnel zones appears negligible in this scenario (see Fig. 12).

However, there is a nonnegligible impact on target areas characterized by a large and smooth surface water extension surrounded by heavy vegetation [31], [32].

## IV. Coherence Detectors

### *A. Introduction: Coherent and Incoherent Scattering Modeling*

There are several correlation techniques to extract the geophysical information from the scattered GNSS signals. CYGNSS uses the classical GNSS-R or cGNSS-R. The scattered electric field is cross-correlated with a replica of the known GNSS codes, so as to generate the so-called complex DDMs (see Fig. 13)

$$Y(\tau, f) = \frac{1}{T_c}\int_0^{T_c} a(t)u(t+\tau)e^{2\pi j(f_c+f)t}dt \quad (16)$$

where $a$ represents the modulating PRN code, $u$ is the received signal, $f_c$ is the GNSS carrier frequency, and $t$ is the time. In a spaceborne scenario, increasing $T_c$ is debatable as the motion of the receiver (∼7 km/s) will limit the signal phase coherence. Some results estimated that close to $T_c = 1$ ms is near optimal and $T_c \sim 0.8$ ms for a faster moving Shuttle instrument [11], while $T_c = 1, 2$ ms for a classical GNSS-R configuration [45]. However, since the scattered signal is of even weaker amplitude than the direct one, and in addition, it suffers from speckle noise, a large number of incoherent averages have to be done to improve the SNR of the so-called power DDMs

$$\left\langle |Y(\tau, f)|^2 \right\rangle = \frac{1}{N_{\text{inc}}}\sum_{i=1}^{N_{\text{inc}}} |Y(\tau, f)|^2 \quad (17)$$

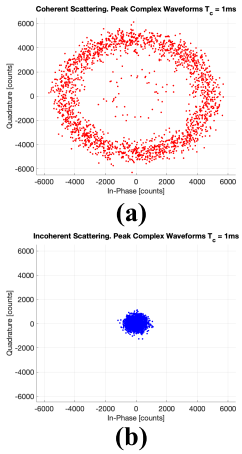



Fig. 13. Scattered complex field (peak of the complex delay waveform, $T_c$ = 1 ms, no incoherent averaging): (a) coherent scattering and (b) incoherent scattering.

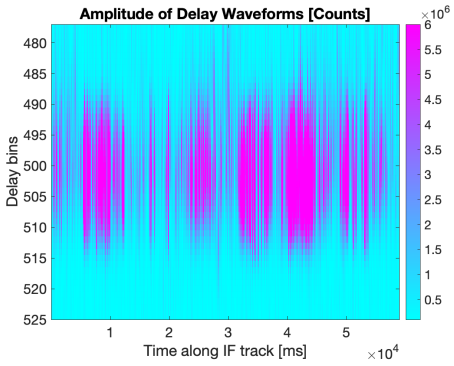



Fig. 14. Sample temporal series of delay vector over the White River Basin, AR, USA (track acquired on January 15, 2022).

Power DDMs can be modeled as the sum of two terms [13], [28], [32], [43]

$$\left\langle |Y(\tau, f)|^2 \right\rangle = \left\langle |Y_{\text{inc}}(\tau, f)|^2 \right\rangle + \left\langle |Y_{\text{coh}}(\tau, f)|^2 \right\rangle \tag{18}$$

where $\langle |Y_{\text{inc}}(\tau, f)|^2 \rangle$ is the incoherent scattering term and $\langle |Y_{\text{coh}}(\tau, f)|^2 \rangle$ is the coherent scattering term.

$\langle |Y_{\text{inc}}(\tau, f)|^2 \rangle$ can be obtained as follows [13]:

$$\left\langle |Y_{\text{inc}}(\tau, f)|^2 \right\rangle = \frac{\lambda^2}{(4\pi)^3} \iint \frac{\text{EIRPG}_r}{R_r^2 R_t^2} \gamma \sigma^0 |X(\tau, f)|^2 dA \tag{19}$$

where $\chi$ is the WAF, $\sigma^0$ is the bistatic scattering coefficient, $\gamma$ is the transmissivity of the vegetation [44], and $A$ is the scattering area, which is limited to the so-called glistening zone.

Under the Huygens–Kirchhoff principle, $\langle |Y_{\text{coh}}(\tau, f)|^2 \rangle$ can be expressed as in (20), shown at the bottom of the page, [29], [30], [31], [32], where $\upsilon$ is is the characteristic free space wave impedance $\sim 120\pi$, $k$ is the angular wavenumber, $\theta_i$ is the incidence angle, $R$ is the complex Fresnel reflection coefficient, and $\sigma$ is the surface height standard deviation (related to small-scale surface roughness).

Results have demonstrated the impact of higher order Fresnel zones on the total coherent reflected power as collected by a GNSS-R sensor, showing ringing fluctuations in the reflected power near high-contrast boundaries. This theoretically determines the spatial resolution of the coherent scattering over heterogenous areas.

### *B. Coherence Detectors: Definitions*

Several coherence indices are provided to help the final users in selecting the most appropriate observable for each targe area, depending on the dominant scattering mechanism, i.e., coherent or incoherent.

The full entropy detector $E_{\text{full}}$ is obtained by applying the von Neumann entropy definition to the corresponding GNSS-R density matrix $D_{\text{full}}$ as follows [46]:

$$E_{\text{full}} = -\text{Tr}(D_{\text{full}} \log D_{\text{full}}) \tag{21}$$

where the symbol Tr is the trace of the matrix.

The full GNSS-R density matrix $D_{\text{Full}}$ is calculated after normalization of the eigenvalues $\beta$ using its trace

$$D_{\text{Full}} = \frac{\beta}{\text{Tr}(\beta)} \tag{22}$$

where $\beta$ is the diagonal eigenvalues matrix generated with the generalized eigen decomposition (GED) of the correlation matrix $Q$

$$\phi^{\text{tp}} Q \phi = \beta \tag{23}$$

where $\phi$ is the eigenvectors matrix and the superscript tp denotes the matrix transpose. $Q$ is generated from the $N$ sequential snapshots of the zero-Doppler delay waveforms $Z$ [$T_c$ = 1 ms and $N_{\text{inc}}$ = 1 ms] (see Figs. 14 and 15) as $Q = ZZ^H/N$, where $H$ denotes the Hermitian transposition. In this study, 48 bins centered at the maximum peak of the waveforms are used for entropy calculations. Tr($\beta$) is equal to the sum of its eigenvalues. $E_{\text{full}}$ output values are finally generated with two different temporal resolutions of 2 and 50 ms.

This metric uses the idea of entropy as an estimation of the information available in the eigenvalues of the correlation matrix. The eigenvalues are a reliable estimator of the energy distributed along the dimensions of the signal subspace. $E_{\text{full}} \sim 1$ represents a uniform eigenvalues' distribution, which is an indication of totally incoherent scattering. On the other hand, $E_{\text{full}} \sim 0$ indicates the presence of a dominant eigenvalue, which is an indication of totally coherent scattering. The full entropy $E_{\text{full}}$ detector is based on the variations in time of the scattered signal, as well as in the shape of the waveforms.

$$\left\langle |Y_{\text{coh}}(\tau, f)|^2 \right\rangle = \upsilon \frac{\lambda^2 G_r \text{EIRP}}{4\pi} \left| -jk \iint \frac{2\cos\theta_i \, X(\tau, f)}{4\pi R_t R_r} \sqrt{\gamma |R|^2 e^{-(2k\sigma\cos\theta_i)^2}} e^{jk(R_t + R_r)} dA \right|^2 \tag{20}$$

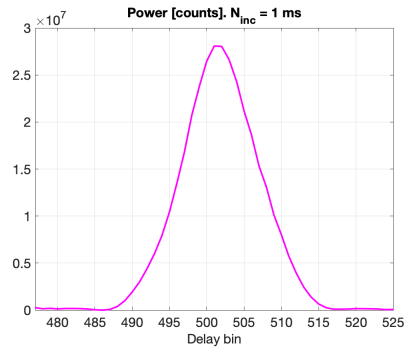



Fig. 15. Sample zero-Doppler delay waveform [$T_c = 1$ ms and $N_{\text{inc}} = 1$ ms] over the White River Basin, AR, USA (track acquired on January 15, 2022).

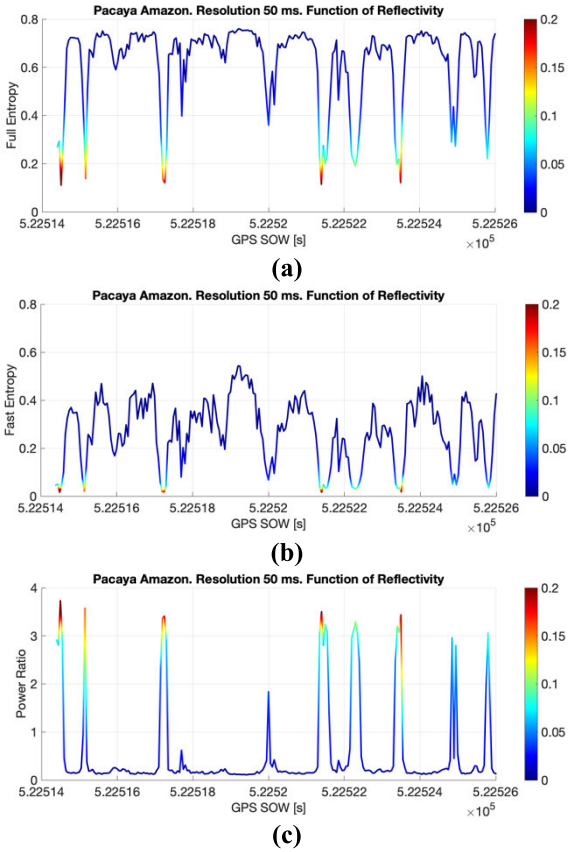



Fig. 16. Coherence detectors time series in Pacaya–Samiria (track acquired on December 31, 2022) as a function of $\Gamma_p$: (a) $E_{\text{full}}$, (b) $E_{\text{fast}}$, and (c) $P_{\text{ratio}}$.

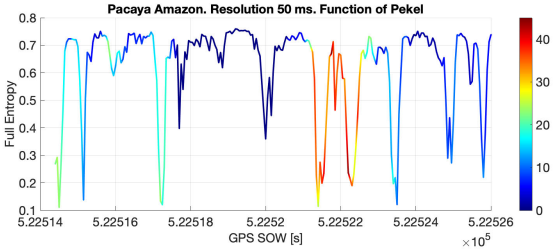



Fig. 17. Comparison of the full entropy $E_{\text{full}}$ coherence detector and the 2-km spatial resolution Pekel surface water percentage [%] over Pacaya–Samiria (track acquired on December 31, 2022).

The fast entropy detector $E_{\text{fast}}$ is a fast and approximated calculation of $E_{\text{full}}$. It is computed using the von Neumann entropy definition as follows:

$$E_{\text{fast}} = -\text{Tr}(D_{\text{fast}} \log D_{\text{fast}}) \tag{24}$$

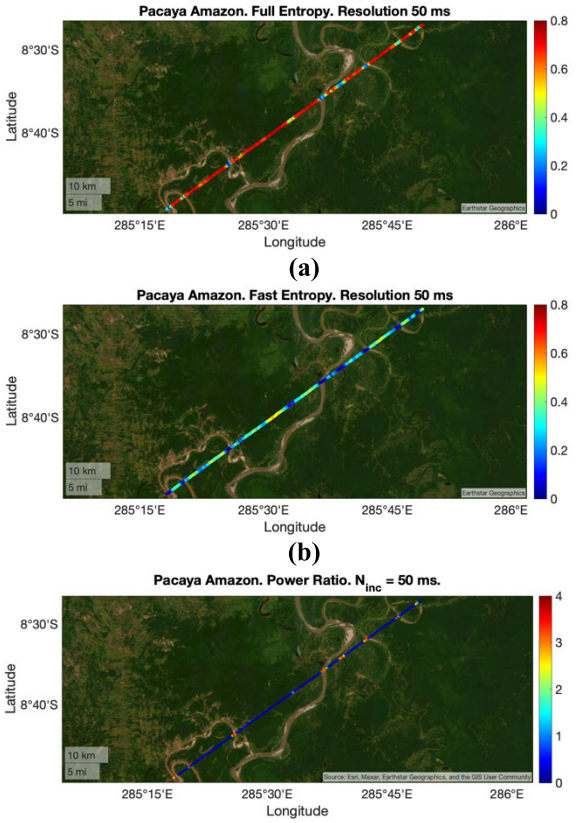



Fig. 18. Coherence detectors geolocated in the Pacaya–Samiria (track acquired on December 31, 2022) for (a) $E_{\text{full}}$, (b) $E_{\text{fast}}$, and (c) $P_{\text{ratio}}$.

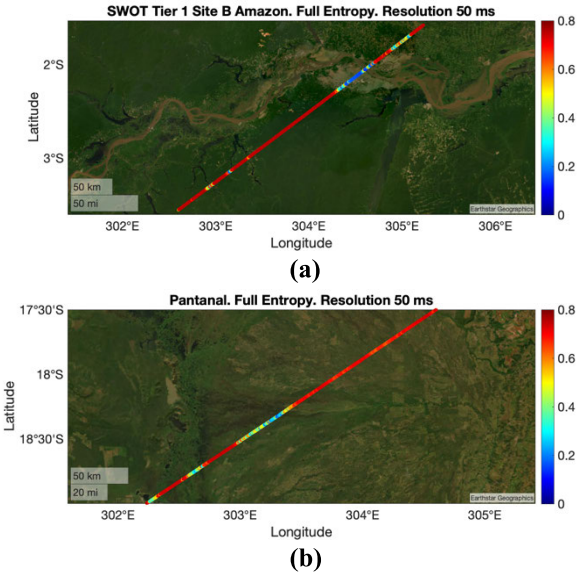



Fig. 19. $E_{\text{full}}$ tracks geolocated in (a) SWOT ca/val site (track acquired on March 27, 2022) and (b) Pantanal (track acquired on July 7, 2022) target areas.

where $D_{\text{fast}}$ is the fast GNSS-R density matrix, which is defined as follows:

$$D_{\text{Fast}} = \frac{\eta}{\text{Tr}(\eta)} \tag{25}$$

where $\eta$ is the diagonal eigenvalues matrix. $\eta_{1,}$ is the largest eigenvalue of the correlation matrix after whitening correlated additive noise $Q_w$, which is computed using the so-called power method [47]. The second eigenvalue $\eta_2$ is

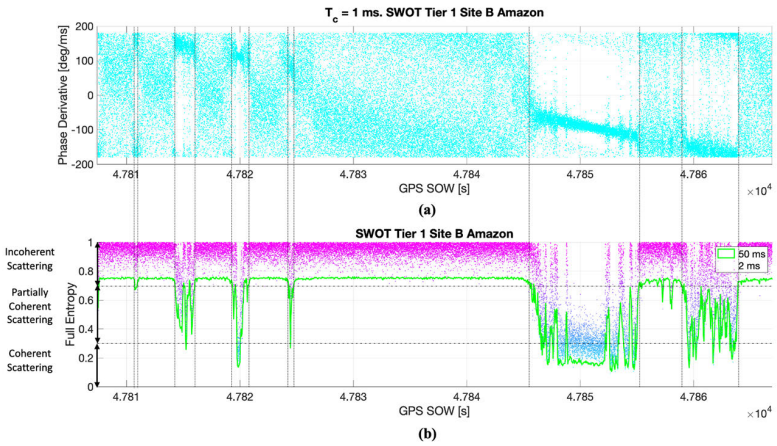



Fig. 20. Time series in the SWOT cal/val site (track acquired on March 27, 2022): (a) $\varphi_{\text{peak}}$ and (b) $E_{\text{full}}$. Full entropy levels are identified for the classification of several scattering regimes: incoherent, partially coherent, and coherent.

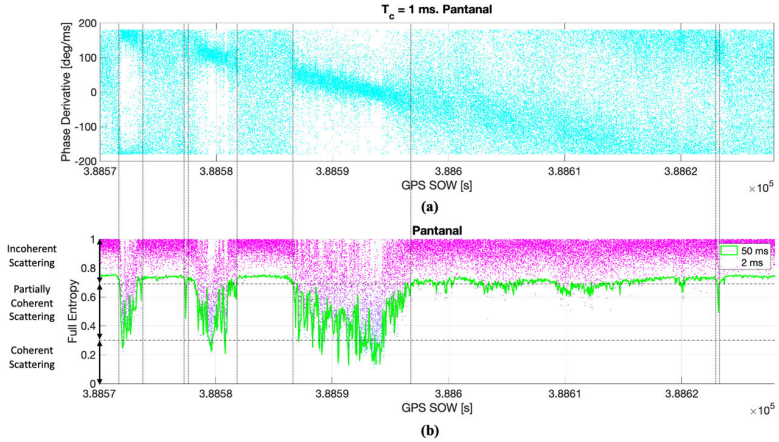



Fig. 21. Time series in the Pantanal (track acquired on July 7, 2022): (a) $\varphi_{\text{peak}}$ and (b) $E_{\text{full}}$. Full entropy levels are identified for the classification of several scattering regimes: incoherent, partially coherent, and coherent.

defined as the mean value of the remaining eigenvalues. The power method is used to iteratively find the eigenvalue of $Q_w$ that is largest in absolute value, i.e., the dominant eigenvalue of $Q_w$. Although this restriction may seem severe, dominant eigenvalues are of primary interest in many physical applications, which is the case.

The power ratio $P_{\text{ratio}}$ is the ratio of the raw counts of the $13 \times 51$ delay Doppler grid surrounding the peak value of $C_{\text{if}}$ [$\Delta f = 50$ Hz and $\Delta\tau = 1/16$ chip] over the sum of the rest of the values as follows [48]:

$$P_{\text{ratio}} = \frac{P_{\text{ratio,in}}}{P_{\text{ratio,out}}} \tag{26}$$

where

$$P_{\text{ratio,in}} = \sum_{i=-6}^{6} \sum_{j=-25}^{25} C_{\text{if}}(\tau_p + i, f_p + j) \tag{27}$$

and

$$P_{\text{ratio,out}} = \sum_{i=1}^{d_w} \sum_{j=1}^{D_w} C_{\text{if}}(i, j) - P_{\text{ratio,in}}. \tag{28}$$

### C. Time Series Analysis: Detectors' Intercomparison

One single raw IF track over a complex heterogeneous scene in the Pacaya–Samiria region is selected to show an intercomparison of the time series of the three coherence detectors previously described (see Figs. 16–18).

The full entropy $E_{\text{full}}$ and fast entropy $E_{\text{fast}}$ suddenly decrease when a water body approaches the nominal specular point because the coherent scattering becomes dominant, and thus, there is a dominant eigenvalue (see Figs. 16 and 18). Consequently, the reflectivity $\Gamma_p$ increases, which is an additional indication that the surface scattering is mainly coherent $\langle |Y_{\text{coh}}(\tau, f)|^2 \rangle$ over surface water bodies [28], [46], [48].

On the other hand, in the presence of vegetated areas, both entropy indices ($E_{\text{full}}$ and $E_{\text{fast}}$) increase because the scattered signal becomes incoherent $\langle |Y_{\text{inc}}(\tau, f)|^2 \rangle$. It is worth pointing out that $E_{\text{full}}$ shows more clear transitions from coherent to incoherent regimes and a higher signal dynamic range than $E_{\text{fast}}$ [see Fig. 16(a) and (b)]. In addition, the power ratio $P_{\text{ratio}}$ time series is depicted [see Fig. 18(c)]. $P_{\text{ratio}}$ increases in the presence of water. $P_{\text{ratio}}$ was designed primarily for use when signal phase information is not available (i.e., the standard CYGNSS L1 products). It has been adapted for its application with short integration times and high delay and Doppler resolution DDMs by tuning the noise exclusion threshold process.

Fig. 17 shows a comparison of the full entropy coherence detector $E_{\text{full}}$ and the 2-km resolution Pekel water mask. $E_{\text{full}}$ provides real-time information regardless of weather

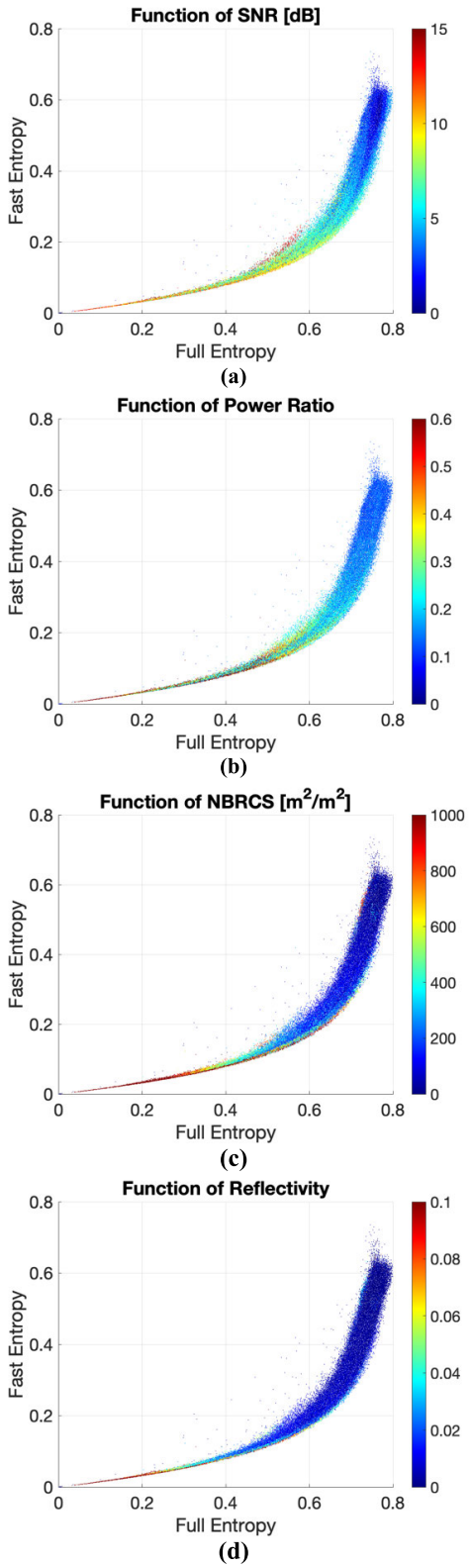



Fig. 22. Scatter plots of $E_{\text{Fast}}$ versus $E_{\text{Full}}$ (resolution 50 ms) using all the available raw IF tracks collected over land surfaces in 2022, as a function of the following parameters with $N_{\text{inc}} = 50$ ms: (a) SNR, (b) $P_{\text{ratio}}$, (c) NBRCS, and (d) $\Gamma_p$.

conditions, while the Pekel mask is based on averaged optical Landsat imagery from the global surface water explorer [49]. This is the reason why the Pekel mask is not able to show the presence of water over areas covered by vegetation (see

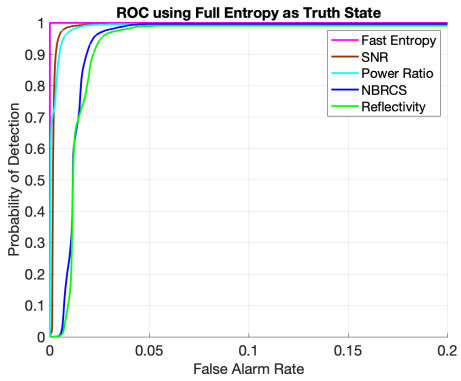



Fig. 23. ROC curves of the peak-observables (SNR, $\Gamma_p$, and NBRCS) and the coherence detectors ($E_{\text{fast}}$ and $P_{\text{ratio}}$) using $E_{\text{full}}$ as the truth reference. Entropy detectors with 50 ms of resolution and the rest of the parameters with $N_{\text{inc}} = 50$ ms.

Fig. 17), while the GED of $Q$ enables the capability to detect small coherence changes (see Fig. 17).

### *D. Full Entropy-Based Coherence Classification*

GNSS-R surface scattering over land surfaces is composed of two terms: coherent $\langle |Y_{\text{coh}}(\tau, f)|^2 \rangle$ and incoherent $\langle |Y_{\text{inc}}(\tau, f)|^2 \rangle$ scatterings, depending mainly on surface roughness [50], [51], [52], [53], [54]. The full entropy $E_{\text{full}}$ is the most powerful coherence detector presented in this study [see Fig. 16(a)]. Here, it is selected as the main truth reference for further evaluation. The phase derivative at the peak of the reflected complex zero-Doppler delay waveforms $\varphi_{\text{peak}}$ is used to derive the full entropy levels that can be used to classify the different scattering regimes. $\varphi_{\text{peak}}$ is computed as the arctangent of the product of the complex peak $Y_n(\tau_p, f_p)$ and the conjugate of the previous complex peak $Y_{n-1}(\tau_p, f_p)$ with $T_c = 1$ ms.

Two raw IF tracks have been selected over target areas with differentiated geophysical properties (see Fig. 19): the first one over the SWOT cal/val site (see Figs. 19(a) and 20) and the second one over the Pantanal [55], [56], which is the world's largest tropical wetland area (see Figs. 19(b) and 21). Both regions are characterized by the presence of surface water covered by heavy upwelling vegetation. This scene remains unresolved for optical sensors.

Three different scattering regimes are shown in Figs. 20 and 21, including incoherent, partially coherent, and coherent. The classification is based on $E_{\text{full}}$ time series with 50 ms of resolution because of the noisier performance with 2 ms. The variance decreases by increasing the number of waveforms (see Fig. 15) for the estimation of each entropy value. The larger the number of waveforms under consideration, the larger the heterogeneity of the equivalent footprint, but the overall entropy is lower. This is relatively similar to speckle noise mitigation by coherent averaging, which increases the coherence of the signal compared to lower $T_c$. In addition, it is worth to comment that the minimum entropy levels are of the same order, independently of the number of waveforms considered for calculations. The incoherent scattering regime is characterized by random phase fluctuations and full entropy levels higher than $E_{\text{full}} \sim 0.7$. This state appears in densely

TABLE II
PER-DDM QUALITY FLAGS 1

| Flag | Definition |
|---|---|
| s_band_powered_up | Set if S-band transmitter is powered up |
| small_sc_attitude_err | Set if the absolute value of the spacecraft roll is between 1 and 30 degrees, the pitch is between 1 and 10 degrees, or the yaw is between 1 and 5 degrees |
| large_sc_attitude_err | Set if the absolute value of the spacecraft roll is greater than or equal to 30 degrees, the pitch is greater than or equal to 10 degrees, or the yaw is greater than or equal to 5 degrees |
| black_body_ddm | Set if the black body load was selected during the DDM sampling period |
| ddmi_reconfigured | Set if the DDMI was reconfigured during the DDM sampling period |
| spacewire_crc_invalid | Set if the DDM CRC transmitted from the DDMI to the spacecraft computer was not valid |
| ddm_is_test_pattern | Set if the DDM is a test pattern generated by the DDMI |
| channel_idle | Set if this reflectometry channel was not tracking a PRN |
| low_confidence_ddm_noise_floor | Set if the difference between this DDM noise floor and the previous DDM noise floor is greater than 10 % |
| sp_over_land | Set if the specular point is over land. Referenced using a map with 0.1 degree lat/lon bins. Coastline features or islands smaller than bin size may not be properly captured |
| sp_very_near_land | Set if the specular point is within 25 km of land. Referenced using a map with 0.1 degree lat/lon bins |
| sp_near_land | Set if the specular point is within 50 km of land. Referenced using a map with 0.1 degree lat/lon bins |
| large_step_noise_floor | Set if the difference between this DDM noise floor and the previous DDM noise floor is greater than 0.24 dB |
| large_step_lna_temp | Set if the LNA temperature rate of change is greater than 1 Celsious degree per minute |
| direct_signal_in_ddm | Set if the absolute value of the difference between direct signal code phase and the DDM signal code phase is less than or equal to four |
| low_confidence_gps_eirp_estimate | Set when there is low confidence in the GPS effective isotropic radiated power estimate |
| rfi_detected | Set when the kurtosis of the DDM noise floor deviates from pure Gaussian by more than 1.0 |
| brcs_ddm_sp_bin_delay_error | Set if the calculated specular point bin delay row is outside of the valid range. This range is different for specular points over land and ocean. The zero-based valid range is greater than 4 (ocean) / 1 (land)and less than 8 (ocean) / 15 (land) |
| brcs_ddm_sp_bin_dopp_error | Set if the calculated specular point bin Doppler column is outside of the valid range. This range is different for specular points over land and ocean. The zero-based valid range is greater than 4 (ocean) / 2 (land) and less than 6 (ocean) / 8 (land) |
| neg_brcs_value_used_for_nbrcs | Set if the BRCS bin used to calculate peak_nbrcs has a negative value |
| gps_pvt_sp3_error | Cannot calculate GPS SV position/velocity/time from SP3 file |
| sp_non_existent_error | Specular point does not exist |
| brcs_lut_range_error | Unable to index into BRCS uncertainty lookup table |
| ant_data_lut_range_error | Unable to index into antenna data lookup table |
| bb_framing_error | Insufficient black body data for calibration |
| fsw_comp_shift_error | Flight software telemetry encoding error of the fsw_comp_delay_shift and fsw_comp_dopp_shift variables. Corrected in FSW version 4.5 |
| low_quality_gps_ant_knowledge | Not enough data is available to properly calibrate the NBRCS for this sample's GPS satellite |
| sc_altitude_out_of_nominal_range | The spacecraft's altitude is out of nominal altitude range. Nominal altitude is defined as between 490 km to 550 km |
| anomalous_sampling_period | Set when an anomaly was observed on the CYGNSS or GPS satellite while this sample was taken. These samples have produced data that do not align with typical CYGNSS results. See up to date list at: https://docs.google.com/spreadsheets/d/1AFAZanVGDApLSnJQAAdPfOKoJQs0jnB8ZvIuD1Z5mAc/edit?usp=sharing |
| invalid_roll_state | The spacecraft's reported roll angle is more than 1 degree from the commanded roll |

vegetated areas without surface water (see Fig. 19). The partially coherent regime is characterized by a noisy linear trend of the phase derivative $\varphi_{\text{peak}}$ and full entropy levels between $E_{\text{full}} \sim 0.3$ and $E_{\text{Full}} \sim 0.7$. This state is found in regions such as the Pantanal wetlands (see Fig. 19). Finally, the coherent scattering regime is found for full entropy levels below $E_{\text{full}} \sim 0.3$. $\varphi_{\text{peak}}$ is clearer in this state, which is associated with the presence of inland water bodies without upwelling vegetation cover, i.e., low $\gamma$ levels. In this scenario, when the surface is smooth, the scattering is highly coherent, and the reflected signal phase can be tracked.

This characterization has been found to provide an accurate scattering classification over the complete CYGNSS raw IF dataset. In this section, two tracks have been selected to illustrate their temporal series, and in Section IV-E, the study is performed using the full dataset.

### *E. Full Dataset Assessment: Fast Versus Full Entropy*

Finally, all the available raw IF tracks collected over land surfaces in 2022 are selected for a global scale assessment. The performance of $E_{\text{fast}}$ versus $E_{\text{full}}$ is evaluated as a function of SNR [see Fig. 22(a)], $P_{\text{ratio}}$ [see Fig. 22(b)], NBRCS [see Fig, 22(c)], and $\Gamma_p$ [see Fig. 22(d)]. $E_{\text{fast}}$ has a lower computational requirement [see (24)] than $E_{\text{full}}$ [see (21)], but there is a clear functional relationship between both entropy metrics. For the coherent scattering regime, i.e., $E_{\text{full}} \sim <0.3$, the relationship appears linear, which means that $E_{\text{fast}}$ is an

TABLE III
PER-DDM QUALITY FLAGS 2

| Flag | Definition |
|---|---|
| incorrect_ddmi_antenna_selection | The wrong (port or starboard) antenna was selected |
| high_signal_noise | The signal is in the highest noise group, but there are still some OK noise rows. Samples are suspect, but may contain quality data. Flag only used for land applications |
| noise_floor_cal_error | The signal is off or is very near the top rows of the full DDM. A proper noise floor cannot be computed. Flag only used for land applications |
| sp_in_sidelobe | The specular point is in the sidelobe causing low confidence in the antenna gain |
| negligible_nst_outage | Minor star track outage with negligible impact on attitude knowledge |
| minor_nst_outage | Minor star track outage with small but acceptable impact on attitude knowledge |
| fatal_nst_outage | Star track outage with unacceptable impact on attitude knowledge |
| low_zenith_ant_gain | Zenith antenna gain is less than -6 dB |
| poor_bb_quality | The distance between the surrounding BB samples > 1350 seconds OR the absolute value of the time to the nearest BB > 350 seconds |
| poor_quality_bin_ratio | Bin ratio on the nadir or zenith antenna is associated with degraded performance |
| low_coherency_ratio | The coherency ratio is below 0.1 on a land sample |
| land_poor_overall_quality | Set if this sample is determined to be of overall poor quality for land applications |
| sp_over_ocean | Set if the specular point is over ocean. Referenced using a map with 0.1 degree lat/lon bins. Coastline features or islands smaller than bin size may not be properly captured |
| sp_extremely_near_ocean | Set if the specular point is within 10 km of ocean. Referenced using a map with 0.1 degree lat/lon bins. When this flag is set the reflectivity_peak and ddm_nbrcs are both considered to be of poor quality |
| sp_very_near_ocean | Set if the specular point is within 25 km of ocean. Referenced using a map with 0.1 degree lat/lon bins. When this flag is set the ddm_nbrcs is considered to be poor quailty, but thereflectivity_peak may still contain good quality data |

excellent coherence detector, despite the use of the power method for the estimation of the dominant eigenvalue. On the other hand, it seems that $E_{\text{fast}}$ saturates for $E_{\text{full}} \sim >0.7$. This is probably because of the better capability of $E_{\text{full}}$ to capture the incoherent scattering regime and its higher signal dynamic range (see Fig. 16). This improved performance is possible because of the higher accuracy of the GED in determining the eigenvalues than numerical methods. $E_{\text{fast}}$ uses the mean value of the remaining eigenvalues, as an estimation of the second eigenvalue $\eta_2$, and thus, there is a limitation in the detection of the incoherent scattering, which is associated with a uniform eigenvalues' distribution.

Higher values of SNR [see Fig. 22(a)], $P_{\text{ratio}}$ [see Fig. 22(b)], NBRCS [see Fig. 22(c)], and $\Gamma_p$ [see Fig. 22(d)] are clustered within the coherent ($E_{\text{full}} \sim <0.3$) and the partially coherent ($0.3 \sim < E_{\text{full}} \sim <0.7$) scattering regimes. To further evaluate the performance of the different observables and coherence detectors, we use the receiver operating characteristic (ROC) curves [8], using $E_{\text{full}}$ as proxy data (see Fig. 23). The scattering is incoherent if the full entropy is $E_{\text{full}} \sim >0.7$, and it is coherent when full entropy is $E_{\text{full}} \sim <0.3$ (see Figs. 20 and 21).

The optimum operating point of an ROC curve is defined at the point of inflection when the slope of each curve crosses from above to below unity (see Fig. 23). This point marks the transition from more true than false detections to more false than true. In addition, the ratio of the probability of detection (PD) and the false alarm rate (FAR) is related to the area between each curve and the diagonal line (PD = 0 & FAR = 0 to PD = 1 & FAR = 1) in Fig. 23: $E_{\text{fast_area}}$ (∼0.49), $\text{SNR}_{\text{area}}$ (∼0.47), and $P_{\text{ratio_area}}$ (∼0.47), $\text{NBRCS}_{\text{area}}$ (∼0.46), and $\Gamma_{p_\text{area}}$ (∼0.46). Based on both the optimum points of the curves and the area under the curves, $E_{\text{fast}}$ shows a behavior almost similar to $E_{\text{full}}$, which confirms the functional relationship found in Fig. 22. The threshold levels (one for each observable) at the optimum operating points of the ROC curves can be used for coherence detection and, thus, for inland water bodies tracking. Future versions of this product could include more coherence detectors [57].

## V. CONCLUSION

The new CYGNSS multiresolution land data product based on enhanced quality DDMs is generated after processing and calibrating raw IF collections. $\Gamma_p$ time series with low integration times, e.g., $N_{\text{inc}} = 2$ and 50 ms, captures land–water transitions with high accuracy because of the higher signal dynamic range and the higher spatial resolution compared to the standard mission L1 product. In addition to power observables, the use of complex DDMs allows us to characterize the performance of more advanced algorithms for coherence detection. Bistatic scattering regimes are classified as incoherent ($E_{\text{full}} \sim >0.7$), partially coherent ($0.3 \sim < E_{\text{full}} \sim <0.7$), and coherent ($E_{\text{full}} \sim <0.3$) by analyzing time series of $\varphi_{\text{peak}}$. Based on this truth reference state generated with $E_{\text{full}}$, ROC curves are used to characterize the performance of $E_{\text{fast}}$, SNR, $P_{\text{ratio}}$, NBRCS, and $\Gamma_p$. A PD higher than ∼95% for an FAR lower than ∼5% is found at the optimum points of the ROC curves using all the 2022 raw IF tracks over land surfaces. In particular, $E_{\text{fast}}$ appears to be an excellent water detector, showing a clear linear functional relationship with $E_{\text{full}}$ under the coherent scattering regime. The lower computational requirement of this detector makes it suitable for in-orbit water monitoring.

The ultimate goal of this article is to show the capabilities of our product to the users for further advancement of the CYGNSS science team investigations over land surfaces, with special interest in inland water bodies monitoring. This is currently a hot research topic with the SWOT mission aiming to resolve ∼100-m-wide rivers and ∼250 × 250 m lakes and reservoirs.

## APPENDIX
## QUALITY FLAGS

See Tables II and III.

## REFERENCES


[1] C. Ruf et al., "CYGNSS: Enabling the future of hurricane prediction [remote sensing satellites]," *IEEE Geosci. Remote Sens. Mag.*, vol. 1, no. 2, pp. 52–67, Jun. 2013, doi: 10.1109/MGRS.2013.2260911.

[2] C. S. Ruf et al., "New ocean winds satellite mission to probe hurricanes and tropical convection," *Bull. Amer. Meteorological Soc.*, vol. 97, no. 3, pp. 385–395, Mar. 2016, doi: 10.1175/BAMS-D-14-00218.1.

[3] C. C. Chew and E. E. Small, "Soil moisture sensing using spaceborne GNSS reflections: Comparison of CYGNSS reflectivity to SMAP soil moisture," *Geophys. Res. Lett.*, vol. 45, no. 9, pp. 4049–4057, May 2018, doi: 10.1029/2018GL077905.

[4] M. P. Clarizia, N. Pierdicca, F. Costantini, and N. Floury, "Analysis of CYGNSS data for soil moisture retrieval," *IEEE J. Sel. Topics Appl. Earth Observ. Remote Sens.*, vol. 12, no. 7, pp. 2227–2235, Jul. 2019, doi: 10.1109/JSTARS.2019.2895510.

[5] M. M. Al-Khaldi et al., "Inland water body mapping using CYGNSS coherence detection," *IEEE Trans. Geosci. Remote Sens.*, vol. 59, no. 9, pp. 7385–7394, Sep. 2021, doi: 10.1109/TGRS.2020.3047075.

[6] J. Zhang, Y. J. Morton, Y. Wang, and C. J. Roesler, "Mapping surface water extents using high-rate coherent spaceborne GNSS-R measurements," *IEEE Trans. Geosci. Remote Sens.*, vol. 60, 2022, Art. no. 4211115, doi: 10.1109/TGRS.2022.3218254.

[7] B. D. Chapman et al., "Comparison of SAR and CYGNSS surface water extent metrics," *IEEE J. Sel. Topics Appl. Earth Observ. Remote Sens.*, vol. 15, pp. 3235–3245, 2022, doi: 10.1109/JSTARS.2022.3162764.

[8] H. Carreno-Luengo and C. S. Ruf, "Mapping freezing and thawing surface state periods with the CYGNSS based F/T seasonal threshold algorithm," *IEEE J. Sel. Topics Appl. Earth Observ. Remote Sens.*, vol. 15, pp. 9943–9952, 2022, doi: 10.1109/JSTARS.2022.3216463.

[9] M. Martín-Neira, "A passive reflectometry and interferometry system (PARIS): Application to ocean altimetry," *ESA J.*, vol. 17, no. 4, pp. 331–355, Dec. 1993.

[10] J. L. Garrison and S. J. Katzberg, "The application of reflected GPS signals to ocean remote sensing," *Remote Sens. Environ.*, vol. 73, no. 2, pp. 175–187, 2000, doi: 10.1016/S0034-4257(00)00092-4.

[11] S. T. Lowe, J. L. La Brecque, C. Zuffada, L. J. Romans, L. E. Young, and G. A. Hajj, "First spaceborne observation of an Earth-reflected GPS signal," *Radio Sci.*, vol. 37, no. 1, pp. 1–28, Jan. 2002, doi: 10.1029/2000RS002539.

[12] A. Camps, "Introduction to remote sensing using GNSS signals of opportunity," in *Ocean Remote Sensing Technologies: High Frequency, Marine and GNSS-Based Radar*. Edison, NJ, USA: IET, 2021. [Online]. Available: https://shop.theiet.org/ocean-remote-sensing-technologies

[13] V. U. Zavorotny, S. Gleason, E. Cardellach, and A. Camps, "Tutorial on remote sensing using GNSS bistatic radar of opportunity," *IEEE Geosci. Remote Sens. Mag.*, vol. 2, no. 4, pp. 8–45, Dec. 2014, doi: 10.1109/MGRS.2014.2374220.

[14] J. Wickert et al., "GEROS-ISS: GNSS reflectometry, radio occultation, and scatterometry onboard the international space station," *IEEE J. Sel. Topics Appl. Earth Observ. Remote Sens.*, vol. 9, no. 10, pp. 4552–4581, Oct. 2016, doi: 10.1109/JSTARS.2016.2614428.

[15] E. Cardellach et al., "GNSS transpolar Earth reflectometry exploring system (G-TERN): Mission concept," *IEEE Access*, vol. 6, pp. 13980–14018, 2018, doi: 10.1109/ACCESS.2018.2814072.

[16] N. Pierdicca et al., "The potential of spaceborne GNSS reflectometry for soil moisture, biomass, and freeze–thaw monitoring: Summary of a European space agency-funded study," *IEEE Geosci. Remote Sens. Mag.*, vol. 10, no. 2, pp. 8–38, Jun. 2022, doi: 10.1109/MGRS.2021.3115448.

[17] E. Loria, A. O'Brien, and I. J. Gupta, "Detection & separation of coherent reflections in GNSS-R measurements using CYGNSS data," in *Proc. IEEE Int. Geosci. Remote Sens. Symp.*, Jul. 2018, pp. 3995–3998, doi: 10.1109/IGARSS.2018.8517441.

[18] W. Li, E. Cardellach, F. Fabra, S. Ribo, and A. Rius, "Assessment of spaceborne GNSS-R ocean altimetry performance using CYGNSS mission raw data," *IEEE Trans. Geosci. Remote Sens.*, vol. 58, no. 1, pp. 238–250, Jan. 2020, doi: 10.1109/TGRS.2019.2936108.

[19] Y. Wang and Y. J. Morton, "Coherent GNSS reflection signal processing for high-precision and high-resolution spaceborne applications," *IEEE Trans. Geosci. Remote Sens.*, vol. 59, no. 1, pp. 831–842, Jan. 2021, doi: 10.1109/TGRS.2020.2993804.

[20] A. Warnock and C. Ruf, "Response to variations in river flowrate by a spaceborne GNSS-R river width estimator," *Remote Sens.*, vol. 11, no. 20, p. 2450, Oct. 2019, doi: 10.3390/rs11202450.

[21] Y. Wang and Y. J. Morton, "River slope observation from spaceborne GNSS-R carrier phase measurements: A case study," *IEEE Geosci. Remote Sens. Lett.*, vol. 19, pp. 1–5, 2022, doi: 10.1109/LGRS.2021.3127750.

[22] S. V. Nghiem et al., "Wetland monitoring with global navigation satellite system reflectometry," *AGU Earth Space Sci.*, vol. 4, no. 1, pp. 16–39, 2017, doi: 10.1002/2016EA000194.

[23] B. Downs, A. J. Kettner, B. D. Chapman, G. R. Brakenridge, A. J. O'Brien, and C. Zuffada, "Assessing the relative performance of GNSS-R flood extent observations: Case study in south Sudan," *IEEE Trans. Geosci. Remote Sens.*, vol. 61, 2023, Art. no. 4201213, doi: 10.1109/TGRS.2023.3237461.

[24] A. Camps, H. Park, J. Castellví, J. Corbera, and E. Ascaso, "Single-pass soil moisture retrievals using GNSS-R: Lessons learned," *Remote Sens.*, vol. 12, no. 12, p. 2064, Jun. 2020, doi: 10.3390/rs12122064.

[25] H. Carreno-Luengo, A. Warnock, and C. S. Ruf, "The cygnss coherent end-to-end simulator: Development and results," in *Proc. IEEE Int. Geosci. Remote Sens. Symp.*, Jul. 2022, pp. 7441–7444, doi: 10.1109/IGARSS46834.2022.9884499.

[26] J. D. Campbell et al., "Intercomparison of electromagnetic scattering models for delay-Doppler maps along a CYGNSS land track with topography," *IEEE Trans. Geosci. Remote Sens.*, vol. 60, 2022, Art. no. 2007413, doi: 10.1109/TGRS.2022.3210160.

[27] M. J. Unwin et al., "An introduction to the HydroGNSS GNSS reflectometry remote sensing mission," *IEEE J. Sel. Topics Appl. Earth Observ. Remote Sens.*, vol. 14, pp. 6987–6999, 2021, doi: 10.1109/JSTARS.2021.3089550.

[28] H. Carreno-Luengo and A. Camps, "First dual-band multiconstellation GNSS-R scatterometry experiment over boreal forests from a stratospheric balloon," *IEEE J. Sel. Topics Appl. Earth Observ. Remote Sens.*, vol. 9, no. 10, pp. 4743–4751, Oct. 2016, doi: 10.1109/JSTARS.2015.2496661.

[29] H. Carreno-Luengo and A. Camps, "Unified GNSS-R formulation including coherent and incoherent scattering components," in *Proc. IEEE Int. Geosci. Remote Sens. Symp. (IGARSS)*, Jul. 2016, pp. 4815–4818, doi: 10.1109/IGARSS.2016.7730256.

[30] A. Camps, "Spatial resolution in GNSS-R under coherent scattering," *IEEE Geosci. Remote Sens. Lett.*, vol. 17, no. 1, pp. 32–36, Jan. 2020, doi: 10.1109/LGRS.2019.2916164.

[31] H. Carreno-Luengo, C. Ruf, A. Warnock, and K. Brunner, "Investigating the impact of coherent and incoherent scattering terms in GNSS-R delay Doppler maps," in *Proc. IEEE Int. Geosci. Remote Sens. Symp.*, Sep. 2020, pp. 6202–6205, doi: 10.1109/IGARSS39084.2020.9324404.

[32] E. Loria, A. O'Brien, V. Zavorotny, B. Downsa, and C. Zuffada, "Analysis of scattering characteristics from inland bodies of water observed by CYGNSS," *Remote Sens. Environ.*, vol. 245, Aug. 2020, Art. no. 111825, doi: 10.1016/j.rse.2020.111825.

[33] H. Carreno-Luengo, C. Ruf, S. Gleason, A. Russel, and T. Butler, "Generation of a new high resolution ddm data product from cygnss raw if measurements," in *Proc. IEEE Int. Geosci. Remote Sens. Symp. (IGARSS)*, Jul. 2021, pp. 7815–7818, doi: 10.1109/IGARSS47720.2021.9554828.

[34] H. Carreno-Luengo et al. *IEEE Standard for Global Navigation Satellite System-Reflectometry (GNSS-R) Data and Metadata Content*, IEEE Standard 4003-2021, IEEE Standards Association, 2021, doi: 10.1109/IEEESTD.2021.9594781.

[35] S. Gleason. *Level 1A DDM Calibration Algorithm Theoretical Basis Document*, CYGNSS Project document 148-0136, Rev 2, Aug. 2018.

[36] S. Gleason and D. Gebre-Egziabher, *GNSS Applications and Methods*. Norwood, MA, USA: Artech House, 2009.

[37] P. Jales, "Spaceborne receiver design for scatterometric GNSS reflectometry," Ph.D. thesis, Univ. Surrey, 2015. [Online]. Available: https://openresearch.surrey.ac.uk/esploro/outputs/doctoral/Spaceborne-receiver-design-for-scatterometric-GNSS/99511677102346

[38] S. Gleason, C. S. Ruf, M. P. Clarizia, and A. J. O'Brien, "Calibration and unwrapping of the normalized scattering cross section for the cyclone global navigation satellite system," *IEEE Trans. Geosci. Remote Sens.*, vol. 54, no. 5, pp. 2495–2509, May 2016, doi: 10.1109/TGRS.2015.2502245.
[39] S. Gleason, C. S. Ruf, A. J. O'Brien, and D. S. McKague, "The CYGNSS level 1 calibration algorithm and error analysis based on on-orbit measurements," *IEEE J. Sel. Topics Appl. Earth Observ. Remote Sens.*, vol. 12, no. 1, pp. 37–49, Jan. 2019, doi: 10.1109/JSTARS.2018.2832981.
[40] S. Gleason, A. O'Brien, A. Russel, M. M. Al-Khaldi, and J. T. Johnson, "Geolocation, calibration and surface resolution of CYGNSS GNSS-R land observations," *Remote Sens.*, vol. 12, no. 8, p. 1317, Apr. 2020, doi: 10.3390/rs12081317.
[41] C. E. Powell, C. S. Ruf, and A. Russel, "An improved blackbody calibration cadence for CYGNSS," *IEEE Trans. Geosci. Remote Sens.*, vol. 60, 2022, Art. no. 1002407, doi: 10.1109/TGRS.2022.3165001.
[42] M. Zribi, K. Dassas, V. Dehaye, P. Fanise, E. Ayari, and M. Le Page, "Analysis of polarimetric GNSS-R airborne data as a function of land use," *IEEE Geosci. Remote Sens. Lett.*, vol. 20, pp. 1–5, 2023, doi: 10.1109/LGRS.2023.3270730.
[43] A. Egido et al., "Airborne GNSS-R polarimetric measurements for soil moisture and above-ground biomass estimation," *IEEE J. Sel. Topics Appl. Earth Observ. Remote Sens.*, vol. 7, no. 5, pp. 1522–1532, May 2014, doi: 10.1109/JSTARS.2014.2322854.
[44] E. Santi et al., "Remote sensing of forest biomass using GNSS reflectometry," *IEEE J. Sel. Topics Appl. Earth Observ. Remote Sens.*, vol. 13, pp. 2351–2368, 2020, doi: 10.1109/JSTARS.2020.2982993.
[45] S. Gleason, "Remote sensing of ocean, ice and land surfaces using bistatically scattered GNSS signals from low Earth orbit," Ph.D. thesis, Univ. Surrey, 2006. [Online]. Available: https://openresearch.surrey.ac.uk/esploro/outputs/99516363402346?institution=44SUR_INST&skipUsageReporting=true&recordUsage=false
[46] I. M. Russo, M. D. Bisceglie, C. Galdi, M. Lavalle, and C. Zuffada, "Entropy-based coherence metric for land applications of GNSS-R," *IEEE Trans. Geosci. Remote Sens.*, vol. 60, 2022, Art. no. 5613413, doi: 10.1109/TGRS.2021.3125858.
[47] S. Andrilli and D. Hecker, *Elementary Linear Algebra*. Amsterdam, The Netherlands: Elsevier, 2010, doi: 10.1016/C2009-0-19744-1.
[48] M. M. Al-Khaldi, J. T. Johnson, S. Gleason, E. Loria, A. J. O'Brien, and Y. Yi, "An algorithm for detecting coherence in cyclone global navigation satellite system mission level-1 delay-Doppler maps," *IEEE Trans. Geosci. Remote Sens.*, vol. 59, no. 5, pp. 4454–4463, May 2021, doi: 10.1109/TGRS.2020.3009784.
[49] J.-F. Pekel, A. Cottam, N. Gorelick, and A. S. Belward, "High-resolution mapping of global surface water and its long-term changes," *Nature*, vol. 540, no. 7633, pp. 418–422, Dec. 2016, doi: 10.1038/nature20584.
[50] E. Motte et al., "GLORI: A GNSS-R dual polarization airborne instrument for land surface monitoring," *Sensors*, vol. 16, no. 5, p. 732, May 2016, doi: 10.3390/s16050732.
[51] A. G. Voronovich and V. U. Zavorotny, "Bistatic radar equation for signals of opportunity revisited," *IEEE Trans. Geosci. Remote Sens.*, vol. 56, no. 4, pp. 1959–1968, Apr. 2018, doi: 10.1109/TGRS.2017.2771253.
[52] N. Pierdicca, L. Guerriero, R. Giusto, M. Brogioni, and A. Egido, "SAVERS: A simulator of GNSS reflections from bare and vegetated soils," *IEEE Trans. Geosci. Remote Sens.*, vol. 52, no. 10, pp. 6542–6554, Oct. 2014, doi: 10.1109/TGRS.2013.2297572.
[53] D. Comite, F. Ticconi, L. Dente, L. Guerriero, and N. Pierdicca, "Bistatic coherent scattering from rough soils with application to GNSS reflectometry," *IEEE Trans. Geosci. Remote Sens.*, vol. 58, no. 1, pp. 612–625, Jan. 2020, doi: 10.1109/TGRS.2019.2938442.
[54] L. Dente, L. Guerriero, D. Comite, and N. Pierdicca, "Space-borne GNSS-R signal over a complex topography: Modeling and validation," *IEEE J. Sel. Topics Appl. Earth Observ. Remote Sens.*, vol. 13, pp. 1213–1218, 2020, doi: 10.1109/JSTARS.2020.2975187.
[55] M. Morris, C. Chew, J. T. Reager, R. Shah, and C. Zuffada, "A novel approach to monitoring wetland dynamics using CYGNSS: Everglades case study," *Remote Sens. Environ.*, vol. 233, Nov. 2019, Art. no. 111417, doi: 10.1016/j.rse.2019.111417.
[56] C. Gerlein-Safdi, A. A. Bloom, G. Plant, E. A. Kort, and C. S. Ruf, "Improving representation of tropical wetland methane emissions with CYGNSS inundation maps," *Global Biogeochemical Cycles*, vol. 35, no. 12, Dec. 2021, Art. no. e2020GB006890, doi: 10.1029/2020GB006890.
[57] E. Loria et al., "Comparison of GNSS-R coherent reflection detection algorithms using simulated and measured CYGNSS data," *IEEE Trans. Geosci. Remote Sens.*, vol. 61, 2023, Art. no. 5105216, doi: 10.1109/TGRS.2023.3277411.



**Hugo Carreno-Luengo** (Senior Member, IEEE) received the Ingeniero Aeronáutico (Plan Antiguo de Estudios, "bachelor's + master's") degree in spacecrafts from the Escuela Técnica Superior de Ingenieros Aeronáuticos (ETSIA), Universidad Politécnica de Madrid (UPM), Madrid, Spain, in 2010, and the Ph.D. degree (cum laude) from the Department of Signal Theory and Communications (TSC), Universitat Politècnica de Catalunya (UPC), Barcelona, Spain, in 2016.

From 2009 to 2010, he performed the final degree project at the Department of Aircrafts and Space Vehicles, UPM. In 2011, he performed the Master of Space Science and Technology at UPC. He was a recipient of a Ph.D. fellowship by the Institut d'Estudis Espacials de Catalunya (IEEC), Barcelona, Spain, where he was involved in the design and development of the first-ever nanosatellite for Earth remote sensing using Global Navigation Satellite System Reflectometry (GNSS-R) from 2011 to 2016. From 2012 to 2015, he was the Principal Investigator (PI) of the TORMES and TORMES 2.0 projects within the European Space Agency's (ESA) REXUS/BEXUS and a Co-PI in the E-GEM FP7 project. From 2013 to 2014, he was a Visiting Researcher with ESA/ESTEC, DLR, Esrange Space Center, Kiruna, Sweden. In the summer of 2016, he was invited by China Great Wall Industry Corporation (CGWIC) to assist with the launch campaign of the $^3$Cat-2 CubeSat at the Jiuquan Satellite Launch Center. From 2016 to 2017, he was a JPL Post-Doctoral Researcher with the National Aeronautics and Space Administration (NASA) Jet Propulsion Laboratory, Pasadena, CA, USA, working in a GNSS-Reflectometry experiment using the radar aboard NASA's SMAP mission. The experiment was successful, which set the basis for the development of a new SMAP operational mode. He was a JdC Post-Doctoral Fellow in the NASA Cyclone Global Navigation Satellite System (CYGNSS) Science Team from 2017 to 2019. Since 2019, he has been a Research Scientist with the College of Engineering, University of Michigan (UMich), Ann Arbor, MI, USA, working directly with the PI of NASA's CYGNSS mission, under a contract with the NASA Science Mission Directorate. He also has the qualification of "Assistant Professor" by the Spanish National Agency for Quality Assessment and Accreditation and "Tenure Track Lecturer" by the Catalan University Quality Assurance Agency. He has participated in 12 international research projects (NASA, ESA, FP7, and so on), being the PI in four and a Co-PI in one of them, managing an estimated budget of 2 M€. He is currently closely involved with NASA's CYGNSS mission, overseeing a total budget of 150 M$ + 39 M$ for the extended mission. He is also contributing as an External Collaborator to the NASA ROSES project. He has participated in three national research projects (MINECO and so on) with a total budget of 1.5 M€, being the PI of two of them. He has also participated in technology transfer activities at CTTC and within the Sesar project [European Union (EU)]. He has advised 13 undergraduate and five master's students. He has managed several student teams within ESA REXUS/BEXUS (ESA Academy). He has reviewed the book *Climate Change and Extreme Events* (Elsevier). He has 50 WoS-indexed publications (41 first + corresponding author). He has published one book chapter (IET) and one IEEE Standard (IEEE SA GRSS). He has provided 64 talks to international research societies, including 14 invited presentations (the IEEE International Geoscience and Remote Sensing Symposium (IGARSS), ESA, and so on). Some of his results have been included on the cover page of the *IEEE GRSS Magazine* (December 2014) and the IEEE JSTARS Special Issue CYGNSS Early on Orbit Performance (January 2019). His research work has attracted 909 citations, reporting an H-index of 23 and an i-10 index of 18. His research interests include the use of GNSS-Reflectometry techniques for Earth remote sensing over land surfaces from small satellites.

Dr. Carreno-Luengo was a member of the Editorial Board of *Earth* (MDPI) from 2020 to 2022. He is a member of IEEE GRSS. He is a member of the Editorial and Reviewer Boards of *Remote Sensing* (MDPI). He held a total of 46 honors and awards, and he has actively participated in numerous outreach activities (national and international). He was a recipient of two IEEE and one NASA Student Travel Grants from 2012 to 2015, an IEEE GRSS Award for the Best Ph.D. Thesis in Geoscience and Remote Sensing, the Serra Hunter Programme, and the CAS's President's International Fellowship Initiative (PIFI) in 2017, the UPC Special Award in Science in 2018, the MDPI Remote Sensing Postdoctoral Award in 2019, and the IEEE SA Standards Board Chair Award in 2021. He was the Session Chair of the 2015, 2017, 2018, 2019, and 2021 IEEE International Geoscience and Remote Sensing Symposium (IGARSS), the 2021 IEEE GNSS+R, and the 2020 NASA CYGNSS Science Team Meeting. He was the Chair of the Town Hall Meeting at IEEE GNSS+R 2021. He is serving as the Chair of the IEEE GRSS Working Group P4003 (Standard for Global Navigation Satellite System-Reflectometry Data and Metadata Content) and the Vice-Chair of the IEEE GRSS Standards for Earth Observation Technical Committee. He was a Guest Editor of various MDPI Remote Sensing Special Issues, including "GNSS-R Earth Remote Sensing

From SmallSats." He has generated 121 reviews in high-impact factor journals, such as IEEE TGRS, IEEE JSTARS, IEEE GRSL, *Remote Sensing* and *Sensors* (MDPI), *Advances in Space Research* (Elsevier), and *Radio Science* (AGU). He has served on the review panel for the NASA ROSES Programme in 2020 and 2023. He has served as an External Reviewer (panelist) for the European Commission and other public research and development centers from EU members in 2020.



**Christopher S. Ruf** (Life Fellow, IEEE) received the B.A. degree in physics from the Reed College, Portland, OR, USA, in 1982, and the Ph.D. degree in electrical and computer engineering from the University of Massachusetts at Amherst, Amherst, MA, USA, in 1987.

He has worked at Intel Corporation, Aloha, OR, USA; Hughes Space and Communication, El Segundo, CA, USA; the National Aeronautics and Space Administration (NASA) Jet Propulsion Laboratory, Pasadena, CA, USA; and Pennsylvania State University, University Park, PA, USA. He is currently the Frederick Bartman Collegiate Professor of climate and space science and the Director of the Space Institute, University of Michigan, Ann Arbor, MI, USA, and a Principal Investigator of the NASA Cyclone Global Navigation Satellite System (CYGNSS) Mission. His research interests include remote sensing technology, methods, and applications.

Prof. Ruf is a member of the American Geophysical Union (AGU) and the American Meteorological Society (AMS) and the Vice-Chair of the Commission F of the URSI. He is a former Editor-in-Chief of the IEEE TRANSACTIONS ON GEOSCIENCE AND REMOTE SENSING. He has served on the editorial boards of *Radio Science*, *Journal of Atmospheric and Oceanic Technology*, and *Scientific Reports*.



**Scott Gleason** (Senior Member, IEEE) received the B.S. degree in electrical and computer engineering from the State University of New York at Buffalo, Buffalo, NY, USA, in 1991, the M.S. degree in engineering from Stanford University, Stanford, CA, USA, in 1999, and the Ph.D. degree in applied physics from the University of Surrey, Surrey, U.K., in 2007.

He is currently the President of Daaxa LLC, a consulting company, Boulder, CO, USA, specializing in global navigation satellite system (GNSS) instruments, calibration, and remote sensing applications. He is a Co-Investigator on the Science Team and an Instrument Scientist for the National Aeronautics and Space Administration (NASA) Cyclone GNSS (CYGNSS) mission. He has worked in the areas of astronautics, remote sensing, and GNSSs for more than 30 years, including at the NASA Goddard Space Flight Center, Greenbelt, MD, USA; the GPS Laboratory, Stanford University, Stanford, CA, USA; Surrey Satellite Technology Ltd., Guildford, U.K.; Concordia University, Montreal, QC, Canada; the Southwest Research Institute; the University Corporation for Atmospheric Research; and the National Oceanography Centre, Southampton, U.K.



**Anthony Russel** received the B.S. degree in computer science engineering from Michigan State University, East Lansing, MI, USA, in 2014.

He is currently a member of the Engineering Staff at the Space Physics Research Laboratory, College of Engineering, University of Michigan, Ann Arbor, MI, USA. His primary engineering activities involve algorithm development and large-scale data processing as a member of the Science Operations Center for the Cyclone Global Navigation Satellite System (CYGNSS) mission.